Immunity

Brief homogeneous TCR signals instruct common iNKT progenitors whose effector diversification is characterized by subsequent cytokine signaling

Graphical abstract

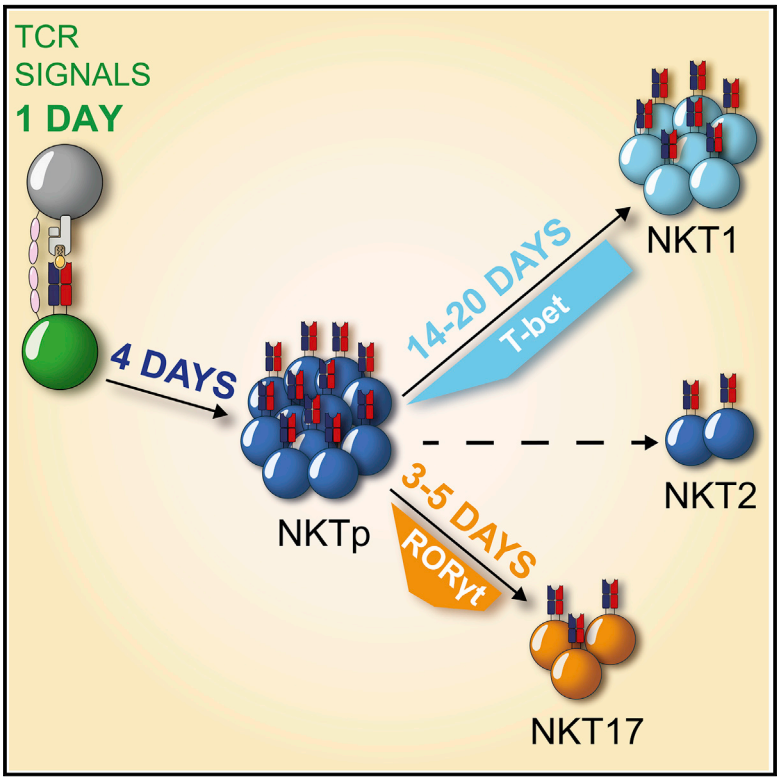

Highlights

- Precise timing of steps and processes driving iNKT cell development
- Homogeneous TCR signals instruct iNKT progenitor, but not effector differentiation
- iNKT subsets emerge simultaneously from the proliferating common progenitor state
- NKT17 identity is acquired in 3–5 days, while NKT1 cells fully mature in 14–20 days

Authors

Sabrina Bortoluzzi, Nyambayar Dashtsoodol, Thomas Engleitner, ..., Tim Ammon, Roland Rad, Marc Schmidt-Supprian

Correspondence

marc.supprian@tum.de

In brief

Innate-like T cells undergo effector differentiation in absence of infection. Leveraging a genetically induced wave of iNKT cell development, Bortoluzzi et al. reveal that early TCR signaling instructs a common progenitor state, while effector subsets emerge later without further TCR input. The precise timing of these events suggests a distinct two-step process for iNKT cell differentiation.

Bortoluzzi et al., 2021, Immunity *54*, 2497–2513
November 9, 2021
https://doi.org/10.1016/j.immuni.2021.09.003

CellPress

Immunity

CellPress

Article

Brief homogeneous TCR signals instruct common iNKT progenitors whose effector diversification is characterized by subsequent cytokine signaling

Sabrina Bortoluzzi,[1,2] Nyambayar Dashtsoodol,[1,2,3,11] Thomas Engleitner,[2,4,5] Christoph Drees,[1,12] Sabine Helmrath,[1,2] Jonas Mir,[6] Albulena Toska,[6] Michael Flossdorf,[6] Rupert Öllinger,[2,4,5] Maria Solovey,[7] Maria Colomé-Tatché,[7,8] Bahire Kalfaoglu,[9] Masahiro Ono,[9] Thorsten Buch,[10] Tim Ammon,[1,2] Roland Rad,[2,4,5] and Marc Schmidt-Supprian[1,2,5,13,*]

[1]Institute of Experimental Hematology, School of Medicine, Technical University of Munich, Munich 81675, Germany
[2]Center for Translational Cancer Research (TranslaTUM), School of Medicine, Technical University of Munich, Munich 81675, Germany
[3]Department of Immunology, School of Biomedicine, Mongolian National University of Medical Sciences, Ulaanbaatar 14210, Mongolia
[4]Institute of Molecular Oncology and Functional Genomics, School of Medicine, Technical University of Munich, Munich 81675, Germany
[5]German Cancer Consortium (DKTK) and German Cancer Research Center (DKFZ), Heidelberg 69120, Germany
[6]Institute for Medical Microbiology, Immunology and Hygiene, Technical University of Munich, Munich 81675, Germany
[7]Institute of Computational Biology, Helmholtz Zentrum München, Neuherberg 85764, Germany
[8]Biomedical Center (BMC), Physiological Chemistry, Faculty of Medicine, LMU Munich, Planegg-Martinsried 82152, Germany
[9]Department of Life Sciences, Imperial College London, London SW7 2AZ, UK
[10]Institute of Laboratory Animal Science, University of Zurich, Schlieren 8952, Switzerland
[11]Present address: Department of Immunology and Stem Cell Biology, Faculty of Medicine, Institute of Medical, Pharmaceutical and Health Sciences, Kanazawa University, Kanazawa, Ishikawa 920-8640, Japan
[12]Present address: Institute for Clinical Chemistry and Pathobiochemistry, Department for Diagnostic Laboratory Medicine, University Hospital Tübingen, Tübingen 72076, Germany
[13]Lead contact
*Correspondence: marc.supprian@tum.de
https://doi.org/10.1016/j.immuni.2021.09.003

SUMMARY

Innate-like T cell populations expressing conserved TCRs play critical roles in immunity through diverse developmentally acquired effector functions. Focusing on the prototypical lineage of invariant natural killer T (iNKT) cells, we sought to dissect the mechanisms and timing of fate decisions and functional effector differentiation. Utilizing induced expression of the semi-invariant NKT cell TCR on double positive thymocytes, an initially highly synchronous wave of iNKT cell development was triggered by brief homogeneous TCR signaling. After reaching a uniform progenitor state characterized by IL-4 production potential and proliferation, effector subsets emerged simultaneously, but then diverged toward different fates. While NKT17 specification was quickly completed, NKT1 cells slowly differentiated and expanded. NKT2 cells resembled maturing progenitors, which gradually diminished in numbers. Thus, iNKT subset diversification occurs in dividing progenitor cells without acute TCR input but utilizes multiple active cytokine signaling pathways. These data imply a two-step model of iNKT effector differentiation.

INTRODUCTION

Unconventional T cells carrying conserved T cell receptor (TCR) repertoires restricted to non-classical major histocompatibility complex (MHC) proteins play important roles in orchestrating innate and adaptive immune cell functions by virtue of their innate-like abilities to rapidly release effector molecules upon activation (Godfrey et al., 2015). Natural killer T (NKT) cells represent a prototypic lineage for multiple innate-like unconventional T cell subsets, including mucosal-associated invariant T (MAIT) cells. Most NKT cells express an invariant TCRα chain arising from rare sporadic Vα14 to Jα18 (Vα14i) rearrangements in mice (Vα24-Jα18 in man) and are referred to as iNKT cells. Several peculiar features of these scarce yet powerful cells distinguish them from mainstream $\alpha\beta$ T cells; these include reactivity to glycolipid antigens presented by MHC-like CD1d proteins and the acquisition of distinct effector/memory-like phenotypes under steady-state conditions entailing the ability to secrete copious amounts of cytokines promptly upon activation (Bendelac et al., 2007; Kronenberg, 2005; Taniguchi et al., 2003). These innate-like features are closely linked to the expression of the key transcription factor promyelocytic leukemia zinc finger (PLZF), which is also found in invariant $\gamma\delta$ T and MAIT cells (Alonzo et al., 2010; Kovalovsky et al., 2008; Savage et al., 2008).

Selection into the iNKT cell lineage occurs in the thymus when $CD4^+CD8^+$ double-positive (DP) and some double-negative (DN) thymocytes expressing a Vα14i-TCR recognize glycolipid antigens presented by CD1d on other DP thymocytes in the context

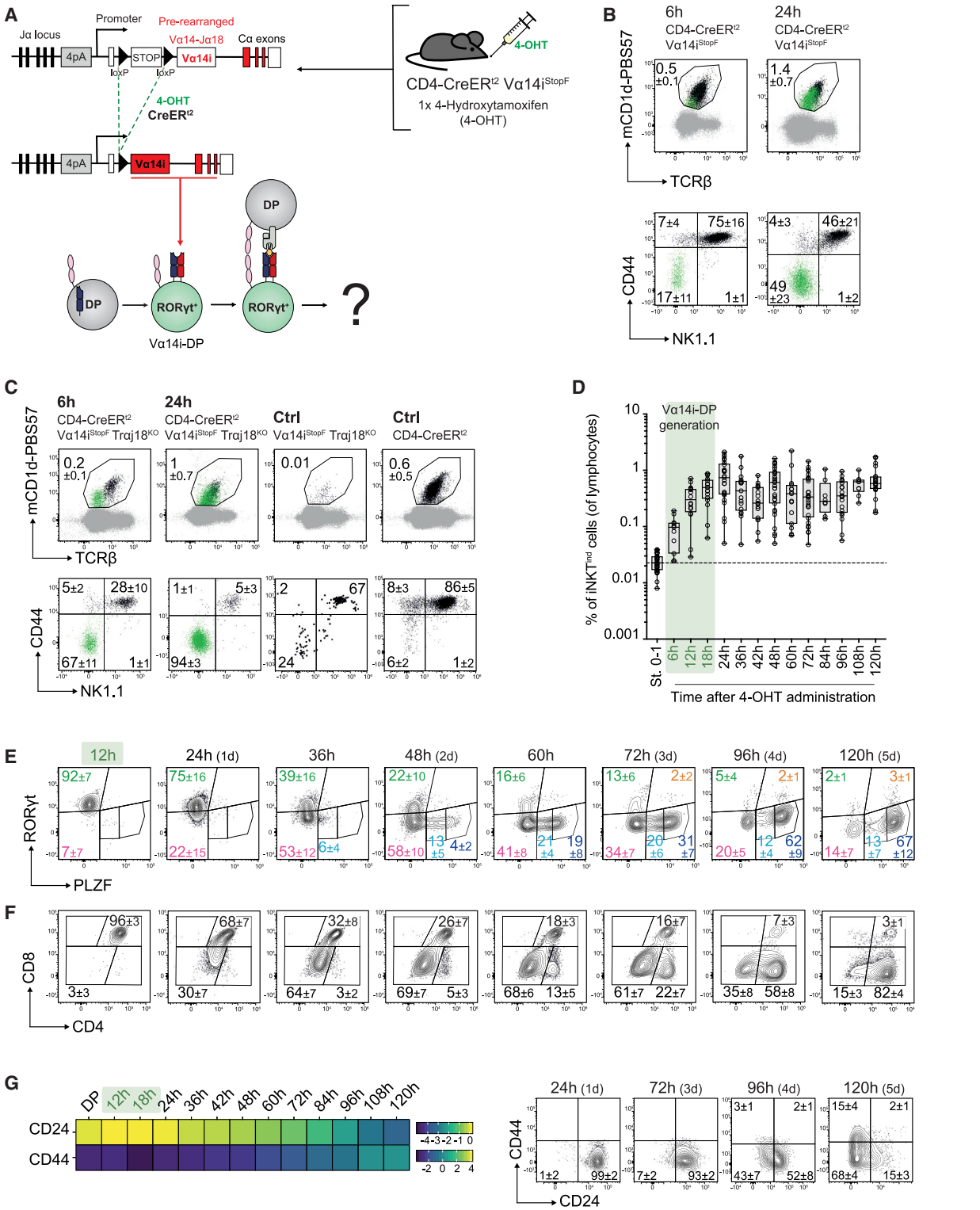

Figure 1. Genetic induction of synchronous iNKT cell development

(A) Schematic representation of the genetic system (blue receptor = TCRβ chain; red receptor = invariant Vα14i-TCRα chain; pink receptor = Slamf; gray receptor = CD1d; yellow ligand = glycolipid).

(B and C) Representative fluorescence-activated cell sorting (FACS) plots of thymocytes (upper rows) and mCD1d-PBS57 Tetramer^{+} iNKT cells (lower rows) from CD4-CreER^{t2} Vα14i^{StopF} (±Traj18^{KO}) mice at 6 and 24 h after TCR induction and the indicated controls. mCD1d-PBS57 Tetramer^{+} NK1.1^{-} CD44^{-} green cells represent newly induced iNKT cells. Numbers indicate the mean percentages ± SD of the gated populations.

(legend continued on next page)

of SLAM-SAP mediated co-stimulation (Dashtsoodol et al., 2019; Griewank et al., 2007). iNKT cell development can be subdivided into the stages 0 ($CD24^+$ $CD44^-$ $NK1.1^-$), 1 ($CD24^-$ $CD44^-$ $NK1.1^-$), 2 ($CD24^-$ $CD44^+$ $NK1.1^-$), and 3 ($CD24^-$ $CD44^+$ $NK1.1^+$) (Bendelac et al., 2007). The iNKT cell TCR can contain a limited number of different TCRβ-chains, but only the invariant α chain contacts the antigen (Borg et al., 2007). Despite this monospecific positive selection, iNKT cells adapt multiple fates during their thymic differentiation resulting in three functionally distinct subsets: NKT1 ($PLZF^{lo}$) with predominant interferon γ (IFN-γ) production potential, interleukin-4 (IL-4) polarized NKT2 ($PLZF^{hi}$), and IL-17 polarized NKT17 ($PLZF^{int}$), which express T-bet, GATA3, and RORγt as respective characteristic transcription factors (Lee et al., 2013). On their journey from a DP thymocyte to effector iNKT cells, two subsequent common precursor and progenitor populations emerge: $CD24^+$ $Egr2^{hi}$ NKT0 and $CD24^-$ $PLZF^{hi}$ $CCR7^+$ $S1PR1^+$ NKTp cells (Hogquist and Georgiev, 2020).

Independent studies propose a central instructive role for TCR signal strength in the fate determination of iNKT cells (Tuttle et al., 2018; Zhao et al., 2018), although how and to what extent remains controversial (Blume et al., 2016; Chen et al., 2017; Henao-Mejia et al., 2013; Lu et al., 2019; Malhotra et al., 2018; Pereira et al., 2014). TCR-mediated effector subset instruction could occur during cortical selection and/or in the medulla following the NKTp stage (Hogquist and Georgiev, 2020).

The rarity of iNKT cell precursors and their sporadic generation remains a critical bottleneck for the analysis of iNKT cell differentiation. Here, we present a detailed pulse-chase analysis of a genetically induced synchronous wave of iNKT cell lineage commitment with ensuing subset diversification *in vivo*. Distinct from pseudo-time or inferred time analyses, we sampled this wave in "real" time points. By monitoring individual differentiation steps, we found that early iNKT cell development is a highly homogeneous process driven by transient uniform TCR signals. iNKT cell subset diversification was initiated at a highly proliferative $PLZF^{hi}$ progenitor stage temporally strictly removed from TCR-mediated activation. Although differentiation was initiated simultaneously, the fates of the three sublineages followed dramatically different trajectories.

Our analyses suggest that innate effector subset diversification is antigen-independent and that lineage instructing signals should occur and therefore be identifiable 4–7 days after initial activation.

RESULTS

Inducing a synchronous wave of iNKT cell development

To systematically investigate the earliest phases of iNKT cell development and subsequent subset differentiation, we aimed to generate an inducible wave of iNKT cell development. In mice bearing CD4-$CreER^{t2}$ (Sledzińska et al., 2013) and $Vα14i^{StopF}$ (Vahl et al., 2013) knockin transgenes, 4-hydroxytamoxifen (4-OHT) administration rapidly led to the expression of a Vα14i-chain containing TCR (Figure 1A). Glycolipid-tetramer (mCD1d-PBS57) staining revealed a clear population of Vα14i-TCR-expressing DP thymocytes (Vα14i-DP) as early as 6 h after 4-OHT gavage (Figure 1B), whose developmental fates could be monitored over time.

To obtain a mouse model fully competent in conventional T cell production but lacking endogenous iNKT cells prior to 4-OHT-mediated Vα14i-DP induction, we generated CD4-$CreER^{t2}$ $Vα14i^{StopF}$ $Traj18^{KO}$ (Cui et al., 1997; Dashtsoodol et al., 2016) mice. A minute fraction of iNKT and T cells were produced in absence of 4-OHT administration. We identified the $Vα14i^{StopF}$ knockin as the source of these "leaky" cells, as they were also present in homozygous $Vα14i^{StopF/F}$ mice in the absence of Cre (Figures 1C and S1A). To exclude mature pre-existing iNKT cells, we gated on $CD44^{lo}$ $NK1.1^-$ iNKT cells (Figure S1B) for early analysis time points (from 6 h to 5 days). Considering the gradual acquisition of CD44 and NK1.1 during iNKT cell maturation, for the 6- to 28-day time points, we marked induced iNKT ($iNKT^{ind}$) cells employing a tdTomato Cre-recombinase reporter (Madisen et al., 2010) (Figure S1B). Developing iNKT cells, which were analyzed between 6 h and 28 days after 4-OHT administration (Figure S1C), reached their highest number 1 day after induction, corresponding to roughly 2% of all thymocytes (Figures 1D and S1D; Table S1).

Thus, our genetic system permitted the precisely timed induction of a sizeable population of Vα14i-DP cells.

Early iNKT cell development proceeds through a $RORγt^-$ $CD4^-$ $CD8^-$ transition toward a $PLZF^{hi}$ $CD4^+$ progenitor state

We conducted kinetic analyses to characterize the fate of the induced iNKT precursors *in vivo*. Twelve h after 4-OHT administration, induced Vα14i-DP cells resembled their DP precursors with respect to RORγt, CD4, CD8, and CD24 levels (Figures 1E–1G and S1E). Vα14i-DP cells first decreased RORγt expression and later started to express PLZF toward a $PLZF^{hi}$ state (Figures 1E and S1E). CD4 and CD8 levels both decreased in parallel to RORγt to reach a transient DN state at 36 h (Figures 1E, 1F, S1E, and S1F). One day later, ThPOK expression (Figures S1G and S1H) was strictly followed by a second wave of CD4 expression (Figures 1F, S1E, and S1F). Concomitantly, CD24 levels were gradually reduced intersecting with a progressive increase of CD44 expression (Figure 1G). At 5 days after induction, nearly all induced cells presented a homogeneous $PLZF^{hi}$ $CD4^+$ $CD24^-$ $CD44^{+/-}$ iNKT phenotype (Figures 1E–1G, S1E, and S1F), demonstrating that we induced a wave of initially synchronous iNKT cell development.

(D) Boxplots showing the proportion of $iNKT^{ind}$ cells of total thymocytes. The boxes extend from the 25^{th} to 75^{th} percentiles, while the whiskers go from the smallest to the largest value. Data are displayed in logarithmic scale. "St. 0-1" indicates Stage 0–1 $CD44^{lo}$ $NK1.1^-$ immature iNKT cells from wild-type mice. (E and F) Representative FACS plots of PLZF/RORγt expression (E) and CD4/CD8 expression (F) in thymic $iNKT^{ind}$ cells. The percentages report means ± SD. (G) Left: median fluorescence intensity (MFI) of CD24 and CD44 in thymic $iNKT^{ind}$ cells. The values were normalized to the expression in DP thymocytes (for CD24) and CD4 SP thymocytes (for CD44). Each time point reports the log2 transformation of mean values. Right: representative FACS plots of CD24 and CD44 expression in thymic $iNKT^{ind}$ cells. Numbers indicate mean percentages ± SD.
Number of replicates, independent experiments, and statistical analyses are reported in Table S2. Time points corresponding to Vα14i-DP iNKT cell generation are highlighted in green here and in subsequent figures. See also Figure S1.

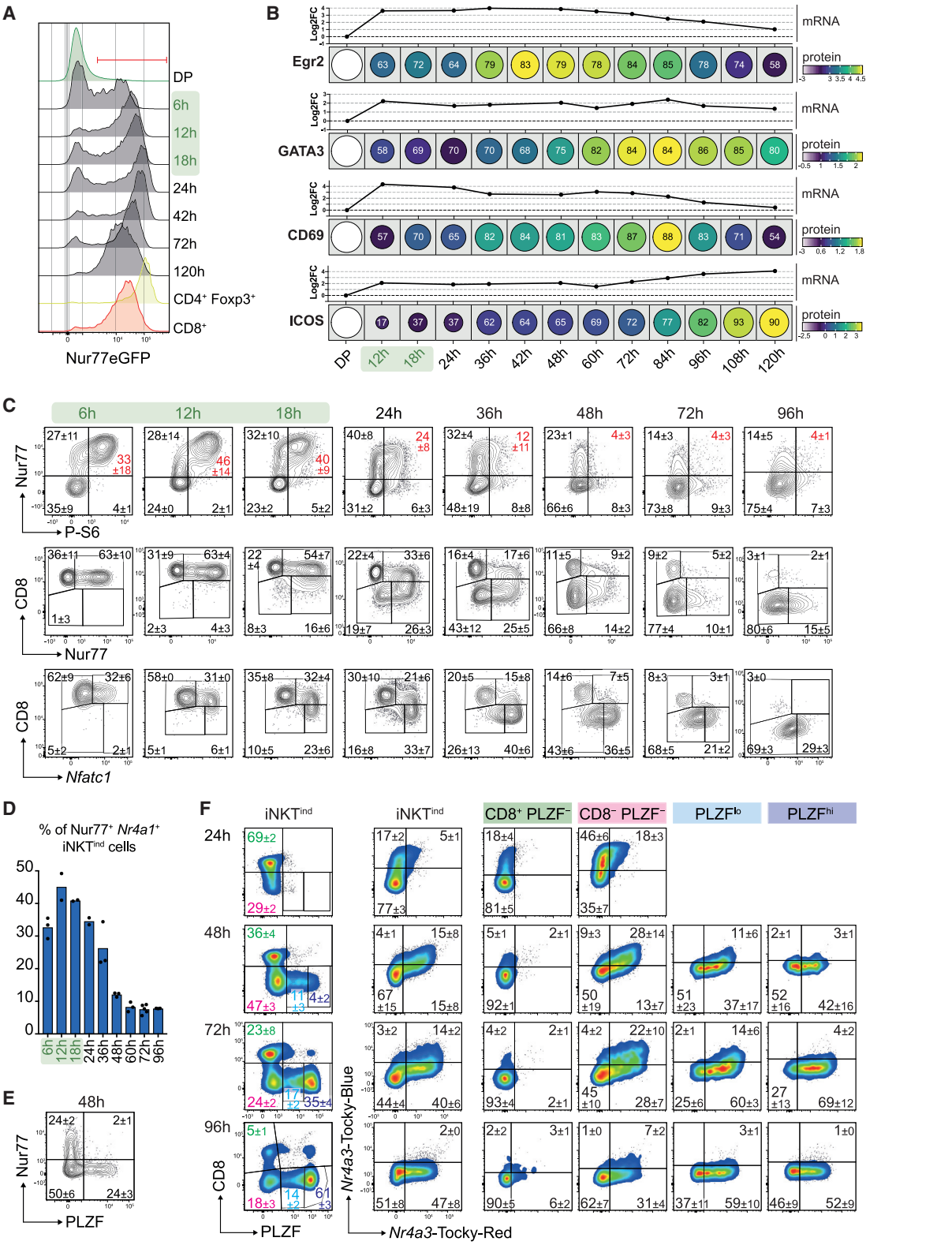

Figure 2. TCR signals instructing iNKT cell positive selection are homogeneous and of short duration

(A) Analysis of TCR signal strength in developing iNKT cells of CD4-CreER^{t2} Vα14i^{StopF} Nur77eGFP (±Traj18^{KO}) mice. The plot displays representative histograms of Nur77eGFP expression in thymic DP thymocytes (DP), iNKT^{ind} cells at different time points, regulatory T cells (CD4$^+$ Foxp3$^+$), and conventional CD8$^+$ T cells (CD8$^+$).

(legend continued on next page)

iNKT cell precursors transiently receive strong homogeneous TCR signals immediately upon TCR-expression

Positive selection by glycolipid antigens initiates iNKT cell differentiation (Bendelac et al., 2007). We therefore investigated TCR signals by means of a Nur77eGFP TCR signal strength reporter (Zikherman et al., 2012). Already at 6 h after Vα14i-TCR induction, roughly 35% of the iNKT^{ind} cells had received a TCR signal, as judged by intermediate levels of Nur77eGFP (Figures 2A and S2A). At 18 h, nearly 70% of the RORγt^{+} iNKT cells contained further elevated Nur77eGFP, and a fraction of RORγt^{lo} cells appeared with higher Nur77eGFP levels. The fraction of RORγt^{lo} cells increased in size and Nur77eGFP intensity, suggesting that the loss of RORγt faithfully marks the positively selected iNKT^{ind} cells (Figure S2A). At 42 h, the Nur77eGFP levels in RORγt^{-} cells peaked at a level corresponding to that of Treg cells (Figure S2B). Nur77eGFP levels then continuously decreased in PLZF-expressing cells over time (Figure S2A). Using the Nur77eGFP robust coefficient of variation (%rCV) as a measure for TCR signal strength dispersion revealed very homogeneous TCR signals in developing iNKT cells with roughly half the dispersion of CD8 SP thymocytes and less than Treg cells, which are also agonist-selected (Figure S2C). Homogeneous and synchronous positive selection was also reflected by the expression of TCR-induced transcription factors and surface markers further downstream: Egr2 expression was closely followed by GATA3, while CD69 expression was followed by PD-1 and then ICOS (Figures 2B and S2D; Table S3).

The long half-life of eGFP impedes the estimation of TCR signal duration using Nur77eGFP mice. Therefore, we employed expression of endogenous *Nr4a1* mRNA and phosphorylation of the S6 protein of the ribosomal S40 subunit (Ma et al., 2020) as well as endogenous Nur77 protein and *Nfatc1* mRNA levels as measures for the strength and duration of TCR signals. We used the rapid loss of CD8 surface levels on iNKT^{ind} cells as a relative measure for developmental time after TCR-mediated activation (Figures 2C and S2E). Our results indicated that all iNKT cells underwent a transient Nur77^{hi} P-S6^{hi} state, indicative of strong antigenic TCR signals, peaking from 12 to 18 h. At 24 h after induction, all CD8^{lo} iNKT^{ind} cells contained homogenously high levels of *Nfatc1* mRNA, indicating that the first CD8^{lo} Nur77^{lo} iNKT^{ind} cells detectable at this time originated from TCR-activated cells. From 24 to 48 h, the fraction of acutely TCR-activated Nur77^{hi} P-S6^{hi} iNKT cells decreased to background levels. We further defined simultaneous high levels of *Nr4a1* mRNA and Nur77 protein as high confidence acute TCR activation (Figures 2D and S6B). The decrease of *Nr4a1*$^{+}$ Nur77^{+} iNKT^{ind} cells over time confirmed the loss of TCR signals from 18 to 48 h. The first emerging PLZF-expressing cells were completely devoid of Nur77 expression, demonstrating a strict temporal separation from TCR signals (Figure 2E). Bulk RNA sequencing of iNKT^{ind} cells at different time points (Figure S2F) fully recapitulated the kinetics of *Nr4a1* and *Nfatc1* mRNA expression detected by flow cytometry. Broader analyses of TCR-induced immediate-early gene signatures revealed that their expression peaked from 12 to 24 h, followed by a constant reduction until 48 or 60 h and a complete loss of expression up to 120 h after iNKT cell induction (Figures S2G and S2H). Leveraging our data on the kinetics of iNKT cell induction and *Nr4a1*, *Nr4a3*, and *Nfatc1* mRNA expression (Figures S1D and S2F; Table S4) into a mathematical model, we calculated that the TCR signaling input received by single iNKT^{ind} cells is best represented as a short pulse that quickly decays with a half-life of less than 8 h (Figure S2I; STAR Methods).

To define TCR signals using another readout, we employed *Nr4a3*-Tocky mice (Bending et al., 2018), which express a fluorescent Timer protein from a TCR-inducible transgenic *Nr4a3* locus. The Timer spontaneously converts from an initially produced unstable blue form to a stable red form with a half-life of 8 h, and the ratio of blue to red protein allows an estimation of the timing and duration of TCR signals: acutely activated cells are blue, recently or persistently stimulated cells are blue/red and upon cessation of the TCR signal the cells enter a red arrested state. We employed PLZFeGFP mice (Zhu et al., 2013) in our Tocky analyses of iNKT^{ind} cells at 24 to 96 h after TCR induction. In the early CD8^{+} PLZF^{-} cells, all the *Nr4a3*-Tocky-expressing iNKT cells were blue, representing cells that recently received a TCR signal (Figures 2F and S2J). At 48 h, cells that lost CD8 expression (CD8^{-} PLZF^{-}) already displayed blue/red Tocky fluorescence. All PLZF^{hi} *Nr4a3*-Tocky-positive iNKT cells were Tocky-red, and comparisons with published signal decay in T cells (Bending et al., 2018) indicated that they were devoid of TCR signals for around 24 h.

Together, the analyses of TCR-induced phosphorylation, mRNA and protein expression, and two genetic reporter systems demonstrated that early iNKT cells receive short highly homogeneous TCR signals immediately upon TCR expression.

(B) Protein and mRNA levels of markers across early iNKT cell development in CD4-CreER^{t2} Vα14i^{StopF} (±Traj18^{KO}) mice. Top (mRNA): log2 fold-change relative to DP thymocytes (FACS-purified as TCRβ^{-} mCD1d-PBS57 Tetramer^{-} CD4^{+} CD8^{+} CD69^{-}) calculated from 3′ RNA sequencing (RNA-seq) data (see STAR Methods; Table S3). Bottom (protein): for each time point, the respective marker-positive fraction of iNKT^{ind} cells was gated, and its MFI calculated. The size of the circles and the number shown inside indicate the percentage of marker^{+} cells of iNKT^{ind} cells, while the color of the heatmap indicates the marker MFI values normalized to the marker MFI of Stage 3 NK1.1^{+} CD44^{+} iNKT cells. For each time point, the heatmap shows a log2 transformation of the mean of the normalized values. (Protein control sample "DP": TCRβ^{-} mCD1d-PBS57 Tetramer^{-} RORγt^{hi} cells).

(C) Representative FACS plots of Nur77/P-S6, CD8/Nur77, and CD8/*Nfatc1*-mRNA (PrimeFlow, see STAR Methods) levels in thymic iNKT^{ind} cells. The percentages report means ± SD.

(D) Percentages of Nur77^{+}/*Nr4a1*-mRNA^{+} thymic mCD1d-PBS57 Tetramer^{+} iNKT^{ind} cells at different time points. The bars show mean percentages, with each data point representing an individual mouse.

(E) Representative FACS plot of Nur77/PLZF expression in thymic iNKT^{ind} cells at 48 h after 4-OHT administration. The percentages report means ± SD.

(F) *Ex vivo* flow cytometric analyses of CD4-CreER^{t2} Vα14i^{StopF} PLZFeGFP *Nr4a3*-Tocky (±Traj18^{KO}) mice at 24, 48, 72, and 96 h after 4-OHT administration. Representative FACS plots show blue-to-red conversion of the *Nr4a3*-Timer protein in the whole thymic induced wave of iNKT cells as well as in the indicated iNKT cell subsets. Numbers indicate mean percentages ± SD.

Number of replicates and independent experiments is reported in Table S2. See also Figure S2.

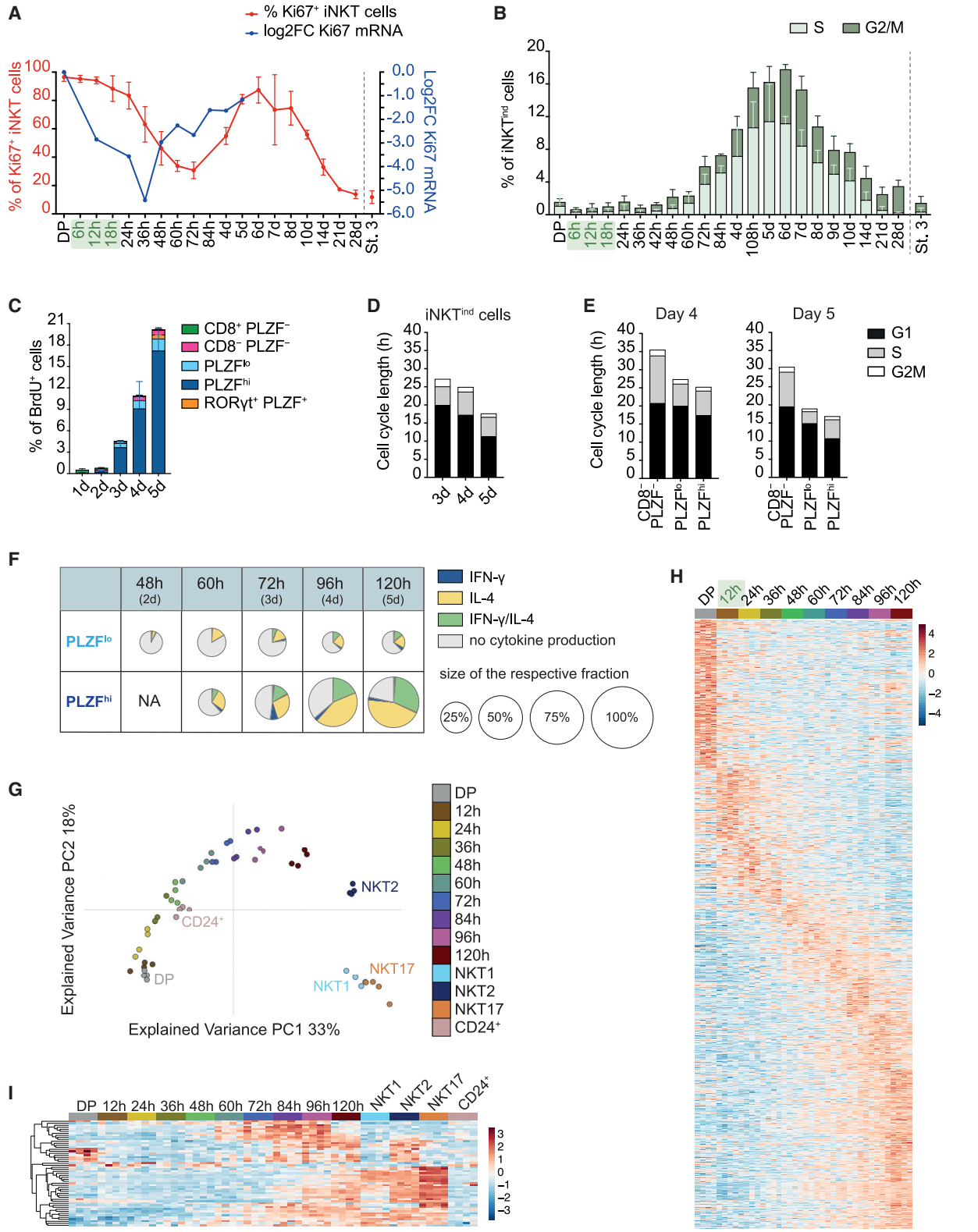

Figure 3. PLZF induction is followed by iNKT cell proliferation, acquisition of cytokine production capabilities and transcription of PLZF-regulated genes

(A) mRNA (determined by 3′ RNA-seq) and protein (measured by FACS) levels of Ki67. mRNA: log2 fold-change to DP thymocytes (FACS-purified as TCRβ⁻ mCD1d-PBS57 Tetramer⁻ CD4⁺ CD8⁺ CD69⁻) calculated from RNA-seq data (see Table S3). Protein: percentages of Ki67⁺ cells in iNKT^{ind} cells, DP thymocytes (gated as TCRβ⁻ mCD1d-PBS57 Tetramer⁻ RORγt^{hi}) and wild-type Stage 3 iNKT cells (St.3). The percentages of Ki67⁺ cells are shown as mean ± SD.

(legend continued on next page)

iNKT cell proliferation is temporally distant from positive selection

Having determined that TCR signaling ceases at the latest 24 h after its expression, we monitored proliferation. While nearly all resting DP thymocytes expressed Ki67 and therefore appeared primed for division, iNKT^{ind} cell precursors lost Ki67 mRNA and with a slight delay protein upon positive selection within the first 36 h after induction (Figure 3A; Table S3). Ki67 was then re-expressed, and DNA content analysis showed that proliferation started at day 3 and reached a maximum at day 5–7, after which it declined until day 14 (Figures 3A and 3B;). *In vivo* BrdU-incorporation experiments confirmed these results (Figure S3A) and revealed that proliferation occurred predominantly in the PLZF^{hi} fraction of developing iNKT cells (Figure 3C). Quantification of cell-cycle speed (Kretschmer et al., 2020) showed that the division time of the iNKT^{ind} cells progressively shortened from 3 to 5 days (Figure 3D) and that PLZF^{hi} cells divided the fastest at all measured time points (Figure 3E).

Overall, our results revealed a delay of 2–3 days between TCR-mediated activation and the proliferation of early iNKT cells, which was mostly restricted to PLZF^{hi} cells.

The acquisition of cytokine production capabilities immediately follows PLZF expression

The functional differentiation of iNKT cells is intimately linked to their ability to produce distinct sets of cytokines upon activation, which we therefore investigated by intracellular flow cytometry (Figures 3F and S3B). Prior to PLZF expression, iNKT cells were unable to produce IL-4, IFN-γ, or IL-17 (Table S5). The first emerging immature PLZF^{lo} cells (day 2 after Vα14i-TCR induction) already contained cells capable of producing IL-4 (Figure 3F). Fittingly, bulk RNA sequencing revealed expression of *Il4* at 48 h and, with a delay of 12 h, *Il13* in iNKT^{ind} cells in absence of *ex vivo* stimulation (Figure S3C; Table S3). High cytokine production potential was predominantly limited to PLZF^{hi} cells, which developed from immature PLZF^{lo} cells 12 h later. From 60 h onward, PLZF-expressing iNKT cells acquired the ability to secrete IFN-γ together with IL-4. At day 5 of development, nearly half of the PLZF^{hi} iNKT^{ind} cells produced IL-4 upon activation, while roughly one-third produced IL-4 and IFN-γ (Figure 3F).

These data showed that the acquisition of iNKT cell cytokine production competence coincides with PLZF expression, precedes the onset of proliferation by 1 day, and steadily increases to reach over 70% IL-4 production competence at day 5 in PLZF^{hi} iNKT cells.

Transcriptional changes of over 3,000 genes characterize early iNKT cell development

We globally investigated the transcriptional changes that guide early iNKT^{ind} cell development between 12 h and 5 days by bulk RNA sequencing, in comparison to DP thymocytes, stage 0 CD24^{+} iNKT cells as well as NKT1, NKT2 and NKT17 mature subsets (Figures 3G–3I and S3D–S3G). Principal-component analysis (PCA) showed clear separation of DP, stage 0, and NKT2, while NKT1 and NKT17 clustered together (Figure 3G). Within the variance represented, the transcriptomes of the iNKT^{ind} cells moved over time from DP toward stage 0, which they reached at the 36–48 h time points, reflecting their developmental trajectory. From there, they appeared to approach the mature stages.

To visualize the extent of significant changes occurring during the first 5 days of development, we identified 3,111 differentially regulated genes within the iNKT^{ind} cell wave, whose mRNA levels were sorted according to their peak at the different time points (Figure 3H; Table S6). The majority of the changes occurred during the earliest developmental phase at the transition from DP to 12 h, corresponding to the onset of TCR signaling and at the transition from day 4 to 5 after induction, when PLZF^{hi}

(B) Frequency of S and G2/M phases of thymic iNKT^{ind} cells at different time points as well as DP thymocytes (RORγt^{hi}) and Stage 3 iNKT cells evaluated by DAPI or DRAQ5 staining. The analysis was performed with the cell cycle algorithm function of FlowJo (Watson Pragmatic Model, constrain: G2 Peak = G1 CV). Data represent means ± SD.

(C) Percentage of individual RORγt/PLZF subsets within BrdU^{+} iNKT^{ind} cells 30 min after BrdU injections. For each time point, the BrdU^{+} fraction of iNKT^{ind} cells was gated, and the distribution of the indicated subsets within the BrdU^{+} fraction was determined. For the PLZF^{-} fraction, RORγt staining was substituted by CD8 staining. Data represent means ± SD.

(D and E) Average cell cycle length (in h) of all thymic iNKT^{ind} cells at day 3, 4, and 5 after induction (D) and of the indicated iNKT^{ind} cells subsets at day 4 and 5 after induction (E). Cell cycle length was computationally calculated using BrdU incorporation data 30 min and 4 h after BrdU injections (see Figure S3A), DNA content measurement, and Ki67 expression information.

(F) Percentages of *ex vivo* activated (4 h with PMA/ionomycin/monensin) thymic PLZF-expressing iNKT^{ind} cells producing the indicated combinations of cytokines measured by flow cytometry. Single, double, and triple producers of IL-4, IFN-γ, and IL-17 were determined by the Boolean tool "Create combinational gates" from FlowJo. IL-17 was measured but not detected at these time points. The size of the pie charts generated with SPICE v6 represents the proportion of PLZF^{lo} and PLZF^{hi} subset of all developing iNKT cells at the different time points. See also Table S5.

(G–I) 1000 cells of the following samples were FACS purified for RNA-seq analyses: 9 time points of iNKT^{ind} cells (from 12 to 120 h) (gated as mCD1d-PBS57-Tetramer^{+} CD44^{lo} NK1.1^{-}); DP = DP thymocytes (TCRβ^{-} mCD1d-PBS57-Tetramer^{-} CD4^{+} CD8^{+} CD69^{-}); CD24^{+} = early wildtype iNKT cells (mCD1d-PBS57-Tetramer^{+} CD44^{-} CD24^{+}); NKT1 (mCD1d-PBS57-Tetramer^{+} CD44^{+} NK1.1^{+} CD27^{+} CD138^{-}); NKT2 (mCD1d-PBS57-Tetramer^{+}, NK1.1^{-} PLZFeGFP^{+} ICOS^{+} IL17RB^{+} CD138^{-}); NKT17 (mCD1d-PBS57-Tetramer^{+} CD19^{-} ICOS^{+} CD138^{+}). For each condition, four biological replicates were sequenced (except for the 96-h time point, where two samples from the same mouse were sequenced). For the NKT17 samples and two NKT2 samples, 2 mice were pooled. For CD24^{+} samples, 4–6 mice were pooled.

(G) Principal-component analysis (PCA) generated with the top 10% most variable genes. Control samples are highlighted in the plot.

(H) The heatmap shows the 3,111 significantly regulated genes sorted according to their maximum expression at each time point. A gene was determined to be differentially regulated if the adjusted p value was below 0.001. See Table S6.

(I) Expression of PLZF-regulated genes across iNKT cell development. The list of PLZF-regulated genes was obtained from Gleimer et al. (2012) and genes upregulated in the comparison of wild-type to PLZF$^{lu/lu}$ mice were used. Out of 96 genes, 67 were detected and 53 were significantly regulated (adjusted p value below 0.001) in our dataset and displayed in the heatmap.

Number of replicates, independent experiments, and statistical analyses are reported in Table S2. See also Figure S3.

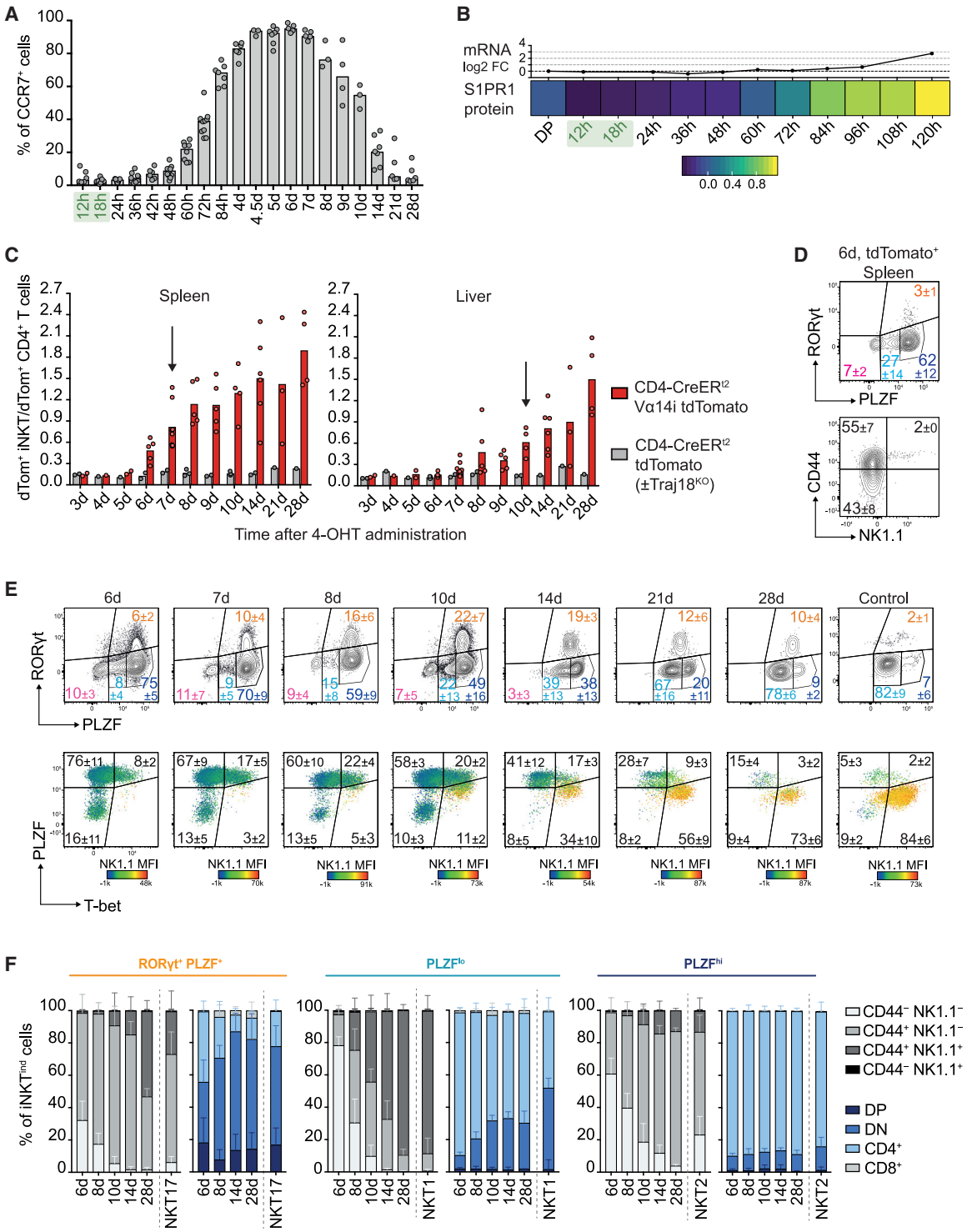

Figure 4. Thymic egress coincides with the start of iNKT cell effector diversification at 6 days after TCR induction

(A) Percentage of thymic CCR7$^+$ mCD1d-PBS57 Tetramer$^+$ iNKT^{ind} cells. Bars indicate median percentages, and each data point represents one mouse.

(B) S1PR1 protein and mRNA levels across iNKT cell development. mRNA levels are shown as log2 fold-change to DP thymocytes calculated from RNA-seq data (see Table S3). For each time point, the MFI of S1PR1 surface protein was normalized to the S1PR1 MFI of TCRβ$^-$ mCD1d-PBS57 Tetramer$^-$ cells. The heatmap shows a log2 transformation of the mean of the normalized values for each time point (Protein control sample "DP": TCRβ$^-$ mCD1d-PBS57 Tetramer$^-$ RORγt^{hi} cells).

(legend continued on next page)

cells dominated. Projecting gene signatures representing early positively selected CD69$^+$ DP thymocytes and stage 1/2 iNKT cells obtained from ImmGen (Heng et al., 2008) onto our wave revealed that gene expression characteristic for positively selected thymocytes was gained at 12–36 h and then progressively lost, while early iNKT cell gene expression was mostly acquired from 72 to 120 h (Figure S3D).

We further divided the significantly regulated genes into 11 unbiased clusters (Figure S3E; Table S6). Correlation to transcription factor expression and pathway-enrichment analysis in the respective clusters yielded loss of DP signature genes for RORγt (cluster 2), enhanced TCR signaling for *Nr4a3* and *Nfatc1* (cluster 4), and translational regulation for PLZF (cluster 10) (Figures S3F and S3G). PLZF-regulated genes (Gleimer et al., 2012) showed significant upregulation within the wave mostly from 72 to 120 h, enriched in clusters 5, 6, and 11 (Figures 3I and S3E).

Together, we provided a global, temporally resolved database of transcriptional changes driving early iNKT cell development *in vivo*.

The developmental time window of thymic egress

Thymic CCR7$^+$ NKTp cells possess the potential to migrate to peripheral sites where they differentiate into mature iNKT cell subsets (Wang and Hogquist, 2018). We observed that the proportion of CCR7-expressing iNKT^{ind} cells started to gradually increase at 42 h to reach 95% between 4.5 and 7 days and consequently decreased to background levels between 14 and 21 days (Figure 4A). Moreover, the expression of S1PR1, which is essential for thymic egress (Allende et al., 2008), was strongly induced between 3 and 5 days of development (Figure 4B).

Corresponding to this time-period, we detected clear populations of tdTomato$^+$ recent thymic emigrant (RTE) iNKT cells in blood and spleen of induced CD4-CreER^{t2} Vα14i^{StopF} tdTomato mice at 6–8 days after induction, while the liver colonization with iNKT cells initiated at 7–10 days (Figures 4C and S4A; the background of pre-existing CD4$^+$ iNKT cells expressing tdTomato upon 4-OHT administration was estimated using CD4-CreER^{t2} tdTomato mice). Splenic tdTomato$^+$ iNKT cells detected 6 days after induction had a prominent PLZF^{hi} CD44$^{+/-}$ NK1.1$^-$ phenotype, confirming that most of them represent RTEs (Figure 4D). Fittingly, at day 6, 85% of splenic tdTomato$^+$ iNKT cells expressed CCR7, which subsequently declined (Figure S4B). Upon arrival, splenic RTE iNKT cells showed moderate proliferation that ceased within 3 days (Figure S4C), indicating that initially, the periphery was mostly populated through thymic egress. Crosses to Traj18^{KO} mice lowered the background of pre-existing iNKT cells and tdTomato$^+$ iNKT^{ind} cells could already be detected in spleen and liver at day 5 and 6, respectively (Figure S4D).

Overall, we identified a window of significant thymic egress, which opened at 5 days after initial Vα14i-TCR expression for 1 week, after which developing iNKT cells became thymus-resident.

A PLZF^{hi} progenitor state represents a turning point between synchronous development and initial subset diversification in 5- to 6-day-old iNKT cells

Our analysis of the first 5 days of iNKT cell development outlined a synchronous and homogeneous developmental program that resulted in a highly uniform, vigorously dividing PLZF^{hi} state.

As the first sign of distinctive subset differentiation, we detected the mutually exclusive expression of RORγt or T-bet in PLZF^{hi} cells at days 5–6 (Figures 4E, S4E, and S4G). These fractions steadily increased both in size and respective transcription factor expression level until days 8–9 and gradually reduced PLZF expression. After day 10, our analyses revealed strikingly different fates between the three iNKT cell subsets: the fraction of RORγt$^+$ iNKT cells contracted, RORγt and PLZF levels decreased to an intermediate level, and the cells acquired a CD4$^-$ CD8$^-$ NK1.1$^{+/-}$ mature NKT17 phenotype (Figures 4E, 4F, and S4E–S4G). On the other hand, T-bet$^+$ iNKT cells continued to expand and to lose PLZF expression to their final low levels at day 28. Furthermore, they acquired NK1.1 and a CD4-to-DN ratio similar to NKT1 cells. The fraction of PLZF^{hi} RORγt$^-$ T-bet$^-$ cells continuously shrank and retained CD4 expression typical of NKTp/NKT2 cells (Figure 4F). The acquisition of high CD44 expression until day 14 was common to all developing iNKT cells (Figures 4F and S4H).

Effector subset identity is acquired quickly in NKT17 and slowly in NKT1 and remains weak in C57BL/6 NKT2 cells

Next, we assessed whether and how quickly the RORγt$^+$ PLZF$^+$ iNKT cells emerging at day 6 acquired NKT17 identity and function. At day 6, 44% of these cells could already produce both IL-4/IL-17 and 19% solely produced IL-17 (Figure 5A). Within 3 to 4 days, the fraction of IL-17 single producers grew to over 50%, and the cells acquired all features of bona fide NKT17 cells within 4 to 5 days, as judged by the cell surface levels of CD138, IL-23R, CD103, and ICOS (Figure 5B).

PLZF^{hi} RORγt$^-$ cells shifted to an IL-4/IFN-γ double-producing phenotype from day 6 to 8 (Figures 5A and S5A), congruent with the increasing T-bet expression within this population. At day 10, the first maturing PLZF^{lo} cells displayed elevated IFN-γ

(C) Ratio of tdTomato$^+$ mCD1d-PBS57 Tetramer$^+$ iNKT cells normalized to tdTomato$^+$ CD4$^+$ T cells in spleen and liver from induced CD4-CreER^{t2} Vα14i^{StopF} tdTomato and control CD4-CreER^{t2} tdTomato (±Traj18^{KO}) mice. The bars report the mean ratios, with each data point representing one mouse. The arrows indicate the first time point at which iNKT^{ind} cells are significantly increased compared to control.

(D) Representative FACS plots of splenic tdTomato$^+$ mCD1d-PBS57 Tetramer$^+$ iNKT^{ind} cells of CD4-CreER^{t2} Vα14i^{StopF} Traj18^{KO} tdTomato mice at day 6 after TCR induction. The percentages represent means ± SD.

(E) Representative FACS plots of PLZF/RORγt and PLZF/T-bet expression in thymic mCD1d-PBS57 Tetramer$^+$ tdTomato$^+$ iNKT^{ind} cells from CD4-CreER^{t2} Vα14i^{StopF} tdTomato (±Traj18^{KO}) mice at different time points and control iNKT cells from CD4-CreER^{t2} mice. The percentages report means ± SD. The color of the PLZF/T-bet dot plots indicates the expression of NK1.1 (as reported in the color scale below). For day 6, only CD4-CreER^{t2} Vα14i^{StopF} Traj18^{KO} tdTomato were used.

(F) Percentages of CD44/NK1.1 and CD4/CD8 subgroups of the indicated developing dTomato$^+$ mCD1d-PBS57 Tetramer$^+$ iNKT cell fractions. Bars indicate mean percentages ± SD. For the PLZF^{lo} subsets, at day 6, only data from CD4-CreER^{t2} Vα14i^{StopF} Traj18^{KO} tdTomato mice were included.

Number of replicates, independent experiments, and statistical analyses are reported in Table S2. See also Figure S4.

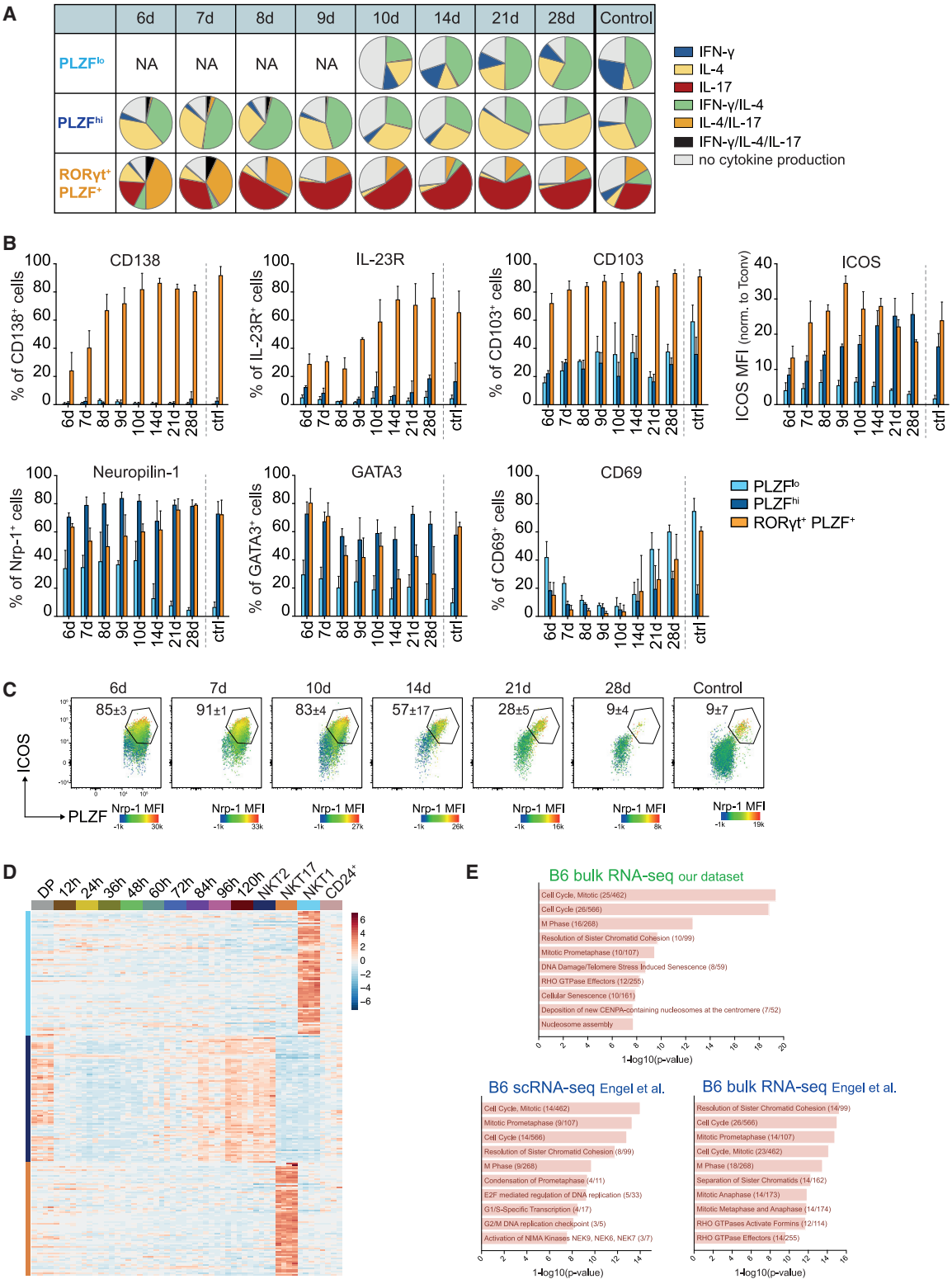

Figure 5. Differentiation trajectories of iNKT cell subset differ dramatically

(A) Percentages of *ex vivo* activated (4 h with PMA/ionomycin/monensin) thymic dTomato$^+$ mCD1d-PBS57 Tetramer$^+$ iNKT^{ind} cells producing the reported combination of cytokines measured by flow cytometry. Single, double, and triple producers of IL-4, IFN-γ, and IL-17 were determined by the Boolean tool "Create combinational gates" from FlowJo. The control sample refers to mCD1d-PBS57 Tetramer$^+$ iNKT cells from CD4-CreER^{t2} (±tdTomato) mice. The pie charts were generated with SPICE v6.

(legend continued on next page)

production potential, and from day 14 onward, consistently over 55% could secrete IFN-γ, with the majority being IL-4/IFN-γ double producers (Figures 5A and S5A). Correspondingly, the fraction of IL-4 single producers increased in the shrinking RORγt$^-$ PLZF^{hi} population, especially at later time points. Monitoring GATA3, Neuropilin-1 (Nrp-1), ICOS, and PD-1 levels did not establish distinct NKT2 differentiation, but their loss coincided with a decrease in PLZF expression and NKT1 differentiation (Figures 5B, 5C, and S5B). From day 14 onward, 60% of PLZF^{hi} iNKT^{ind} cells showed a PD-1$^+$ CCR7$^-$ phenotype (Figure S5B) typical for mature NKT2 cells in BALB/c mice (Wang and Hogquist, 2018). The expression dynamics of CD69 recapitulated a two-step thymic iNKT cell development: CD69 levels initially uniformly increased in response to strong selecting TCR signals, reaching a peak at 84 h (Figure 2B). The fraction of CD69$^+$ cells then continuously shrank until day 10, when a second expression wave appeared to follow subset differentiation in the majority of NKT1 and NKT17, but only a few PLZF^{hi} cells (Figure 5B).

Together, a picture emerged that PLZF^{hi} RORγt$^-$ cells continuously differentiated toward a NKT1 fate, at the expense of maturing NKT2 cells that disappeared over time.

To identify potential earlier functional iNKT cell subset differentiation, we extracted signature gene lists for the NKT1, NKT2, and NKT17 subsets from our and published (Engel et al., 2016; Lee et al., 2016) transcriptomes (Table S7) and highlighted their expression in the induced iNKT cell wave (Figures 5D and S5C). While NKT1 and NKT17 signature genes were largely absent from the induced wave, NKT2 signature genes were enriched in the predominantly PLZF^{hi} day 5 iNKT^{ind} cells (Figures 5D and S5C). This could be explained by the fact that C57BL/6 NKT2 signature gene lists were dominated by cell cycle genes (Figure 5E). In contrast, BALB/c NKT2 gene signatures (Lee et al., 2016) were not detected in developing iNKT cells at day 5 (Figure S5C) and did not show any enrichment in cell cycle genes (data not shown). Along this line, the comparison of C57BL/6 to BALB/c NKT2 gene signatures revealed very little overlap (Figure S5D). Next, we attempted to identify genes marking NKT2 maturation by focusing on the genes differentially expressed between iNKT^{ind} cells at day 5 and wild-type NKT2. However, all of these genes were similarly expressed also in NKT1, NKT17, or both NKT1 and NKT17 (Figure S5E), suggesting that in C57BL/6 mice, NKT2 cells lacked a strong specific gene signature.

Effector subset diversification is not linked to TCR signals but to small differences in overall strong cytokine responses

We did not observe any evidence for fate-changing TCR signals in iNKT^{ind} cells between day 5 and 28 of their development using methods optimal for the acute detection of transient signals (Figures 6A, 6B, S6A, and S6B) or capable of displaying transiently received signals for long periods of time (Figures 6B and S6C). Therefore, we next quantified the phosphorylation of Stat5, Smad2/3, and Stat3 (Figure 6C)—key signal transducers downstream of cytokines implicated in effector differentiation, among them IL-15, TGF-β, and IL-25 (Wang and Hogquist, 2018). Stat5 is phosphorylated in response to IL-15 (Pandiyan et al., 2012), which is highly expressed by medullary thymic epithelial cells (Cui et al., 2014) and implicated in NKT1 cell survival, proliferation, terminal differentiation, and T-bet expression (Gordy et al., 2011; Matsuda et al., 2002). Phosphorylation of Stat5 during iNKT^{ind} cell development occurred strictly in parallel with PLZF expression starting at 36 h and was uniformly high in PLZF^{hi} iNKT^{ind} cells at day 4 and 5, indistinguishable from the very first emerging RORγt- and T-bet-expressing cells (Figure 6C). Elevated levels of phosphorylated Smad2/3 indicated ongoing TGF-β signaling in RORγt$^+$ NKT17 cells, which, accordingly, fully depend on TGF-βRII expression (Havenar-Daughton et al., 2012). Smad2/3 phosphorylation increased at day 3 in PLZF-expressing iNKT^{ind} cells and peaked in PLZF^{hi} cells at day 4 and 5, when RORγt$^+$ iNKT cells contained slightly higher P-Smad2/3 levels compared with T-bet$^+$ PLZF^{hi} cells. From day 8 onward, RORγt$^+$ iNKT cells signaled consistently more through Smad2/3 than the other iNKT subsets (Figure 6C). Stat3, which can be activated by IL-25, is critical for Th17 differentiation, but its relevance for NKT and NKT17 cells differ between humans (Wilson et al., 2015) and mice (St Leger et al., 2018), where it is dispensable. Tracking Stat3 activation showed that its phosphorylation initially correlated with PLZF expression and was further elevated in RORγt$^+$ and T-bet$^+$ iNKT cells at day 5 and 6—followed by a decrease, especially in T-bet$^+$ PLZF^{lo} iNKT cells.

iNKT^{ind} cells start to egress the thymus at 5 days after induction (Figures 4C, 4D, and S4D). Similar to the thymus, the proportion of splenic mature iNKT^{ind} cells increases over time, most likely because of local maturation and thymic influx of more mature cells (Figures S7A–S7D). At later time points, we detected a larger fraction of maturing PLZF^{lo} IFN-γ-only producers in the spleen, probably reflecting the presence of diverse local factors affecting differentiation or homeostasis (Figure S7E).

Together, our results revealed that iNKT subset differentiation starts 5 days after positive selection in two distinct phases in absence of detectable TCR signals (Figure 7A). The first phase, lasting from day 5 to 10, was characterized by generally high cytokine signaling and a burst of acute RORγt and T-bet upregulation on dividing PLZF^{hi} progenitor cells. In the case of RORγt, which progressively instructed complete NKT17 lineage identity

(B) Percentages of thymic dTomato$^+$ mCD1d-PBS57 Tetramer$^+$ iNKT^{ind} cell subsets expressing CD138, IL-23R, CD103, Neuropilin-1, GATA3, and CD69. Bars show mean percentages ± SD. Part of the control data were previously published (Drees et al., 2017). For ICOS, the bar graph reports the MFI of the indicated iNKT^{ind} cell subsets normalized to the ICOS MFI of conventional T cells (TCRβ+ mCD1d-PBS57 Tetramer$^-$).

(C) Representative FACS plots of ICOS and PLZF expression in thymic PLZF$^+$ RORγt$^-$ mCD1d-PBS57 Tetramer$^+$ iNKT^{ind} cells from CD4-CreER^{t2} Vα14i^{StopF} tdTomato (±Traj18^{KO}) mice as well as control iNKT cells from CD4-CreER^{t2} mice. Numbers indicate mean percentages ± SD. The color of the dot plots indicates the intensity of the expression of Neuropilin-1 (reported in the scale below).

(D) mRNA expression of NKT2 (dark blue), NKT17 (orange), and NKT1 (light blue) signature genes across iNKT cell development. Subset-specific signature gene lists were calculated from our RNA-seq dataset (see STAR Methods; Table S7).

(E) Pathway-enrichment analysis performed with EnrichR of NKT2 signature genes identified in our dataset, as well as from a published dataset (Engel et al., 2016). Pathways were selected for adjusted p value < 0.05 and the top 10 pathways were depicted.

Number of replicates, independent experiments, and statistical analysis is reported in Table S2. See also Figure S5.

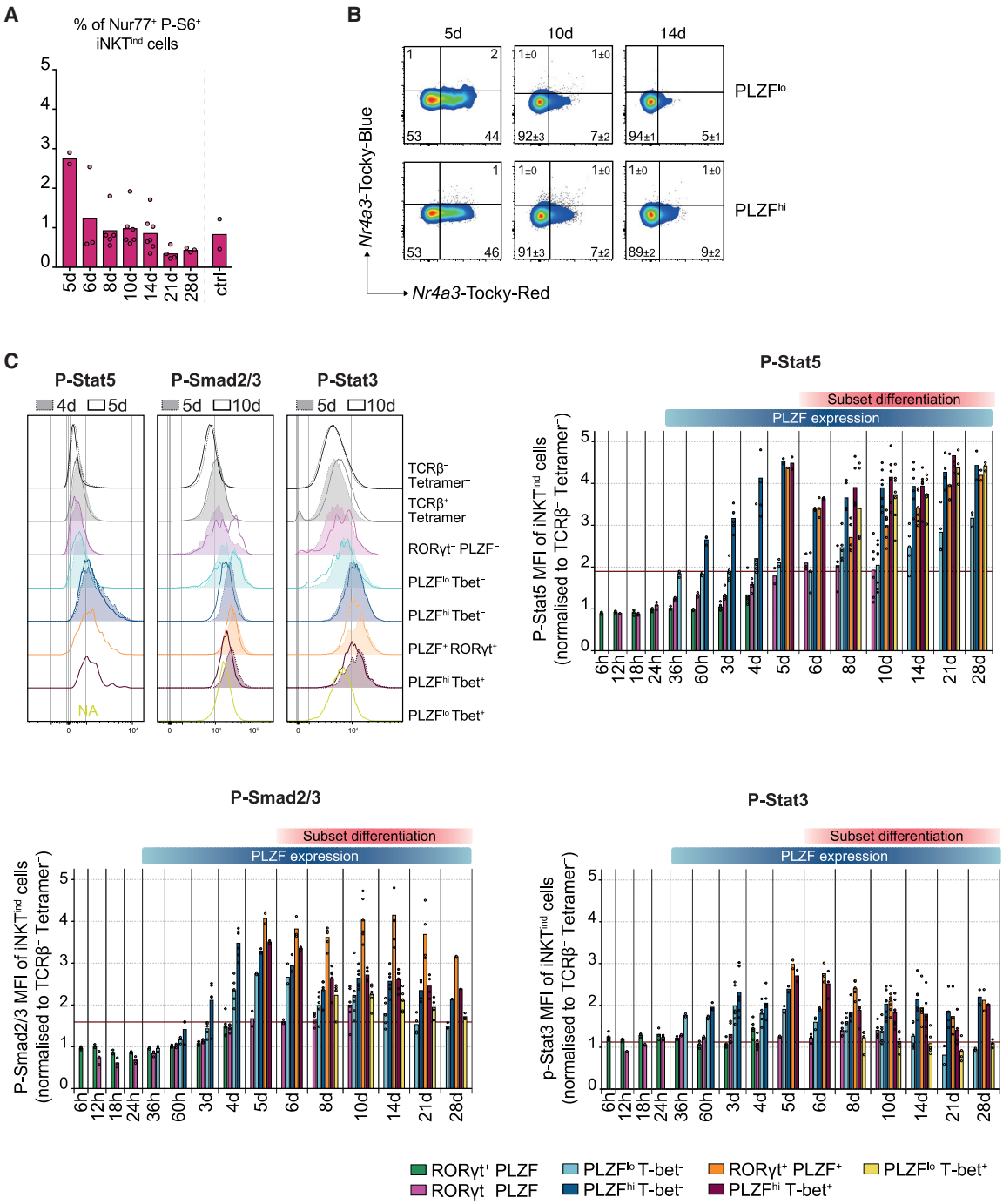

Figure 6. Absence of TCR signals and elevated phosphorylation of cytokine-induced signal transducers in late-developing iNKT cells

(A) Percentages of Nur77+/P-S6+ thymic mCD1d-PBS57 Tetramer$^+$ iNKT^{ind} cells and control wild-type iNKT cells. The bars show mean percentages, with each point representing an individual mouse.

(B) *Ex vivo* flow cytometric analyses of CD4-CreER^{t2} Vα14i^{StopF} Traj18^{KO} PLZFeGFP *Nr4a3*-Tocky mice at day 5, 10, and 14 after 4-OHT administration. Representative FACS plots show blue-to-red conversion of the *Nr4a3*-Timer protein in thymic PLZF^{lo} and PLZF^{hi} iNKT^{ind} cell subsets. Numbers indicate mean percentages ± SD.

(C) Top left graph: representative histograms showing the levels of phosphorylated Stat5, Smad2/3, and Stat3 in thymic mCD1d-PBS57 Tetramer$^+$ iNKT^{ind} cells at the indicated time points. Top right and bottom graphs: MFI of P-Stat5, P-Smad2/3, and P-Stat3 in mCD1d-PBS57 Tetramer$^+$ iNKT^{ind} cells subsets. For each sample, the MFI of iNKT^{ind} cell subsets was normalized to the MFI of TCRβ$^-$ mCD1d-PBS57 Tetramer$^-$ thymocytes. The bars report the mean of the normalized values. For each graph, the red horizontal line indicates the mean MFI of TCRβ$^+$ mCD1d-PBS57 Tetramer$^-$ T cells. For the time points between day 8 and 28, only CD4-CreER^{t2} Vα14i^{StopF} Traj18^{KO} mice were used.

Number of replicates, independent experiments, and statistical analyses are reported in Table S2. See also Figures S6 and S7.

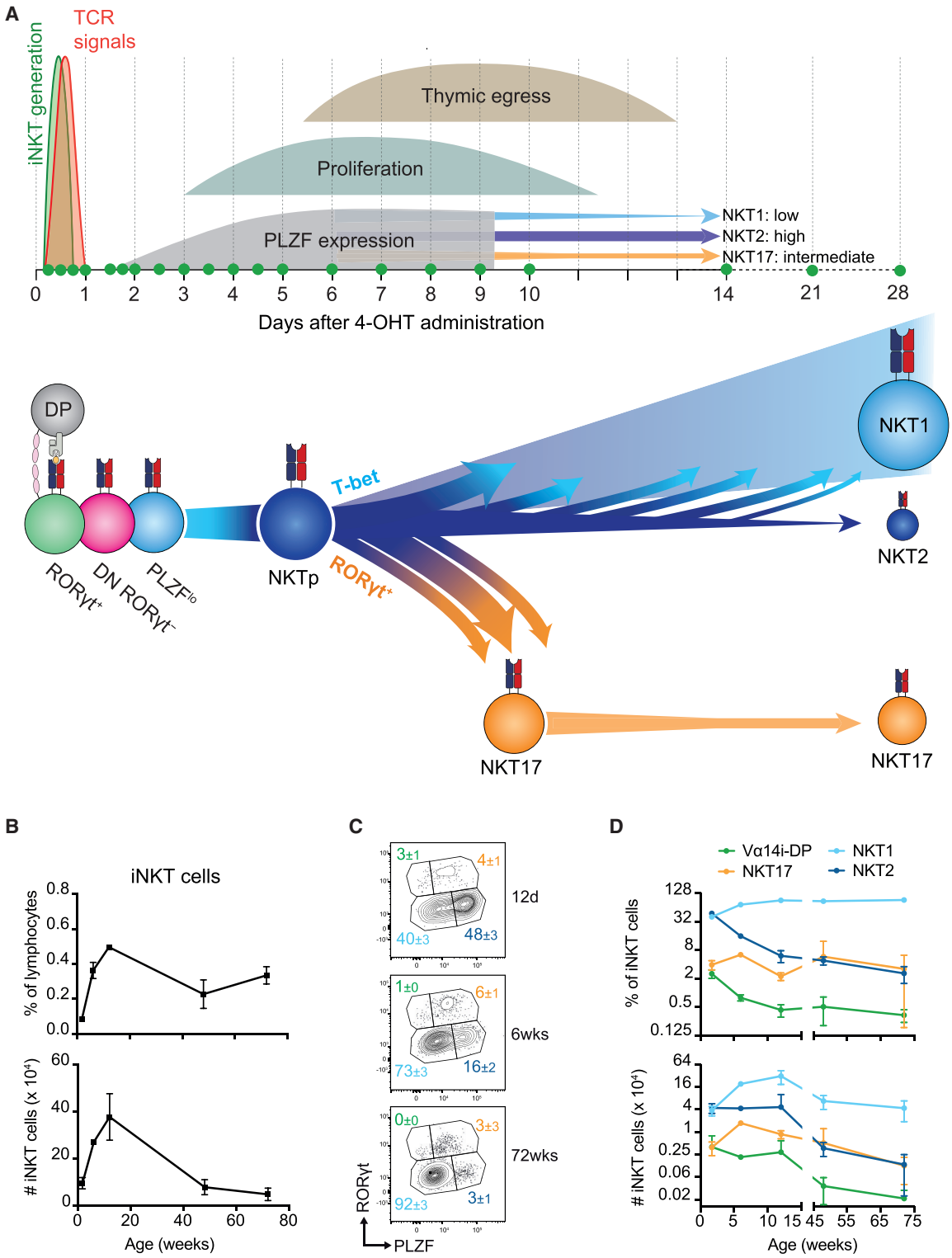

Figure 7. Age-dependent distribution of iNKT cell subsets

(A) Model of iNKT cell development and differentiation.

(B) Percentage (upper graph) and absolute cell number (lower graph) of thymic iNKT cells isolated from C57BL/6 mice at the indicated ages. Data show mean ± SD.

(legend continued on next page)

within a 3-to-5-day period, this process was correlated to ongoing signaling through Smad2/3, and it was the only source of NKT17 cells. In contrast, T-bet^{+} cells only slowly acquired the full NKT1 identity, and the NKT1 cell pool was continuously fueled by differentiation of NKT2-like PLZF^{hi} cells.

To evaluate whether our induced iNKT cell wave reflected endogenous iNKT cell differentiation, we analyzed steady-state effector subset composition in juvenile and adult mice (Figures 7B–7D and S7F). At 12 days of age, when comparatively large numbers of the earliest Vα14i-DP iNKT cells indicated high rates of production, iNKT effector subset composition was closer to the earlier time points in our wave. As mice aged and iNKT generation decreased, effector subset composition more closely resembled iNKT^{Ind} cells of the later time points.

DISCUSSION

iNKT cells belong to a larger group of invariant and innate-like T cell subsets, which acquire distinct effector functions in the absence of infection early on during development (Hogquist and Georgiev, 2020). Our analyses suggested that the journey of newborn iNKT cell precursors toward adult effector cells (see Figure 7A) comprises three distinct phases: (1) transient homogeneous TCR signals, (2) a highly proliferating homogeneous PLZF^{hi} progenitor state, and (3) subsequent effector subset differentiation.

Immediately upon TCR expression, Vα14i-DP cells experienced a TCR signal that is uniform and of short duration. The immediate response indicated that DP thymocytes able to transmit positive selection signals to Vα14i-DP thymocytes were highly abundant. We estimated that 90% of the TCR signaling input of Vα14i-DP cells was lost within 24 h after initial activation.

TCR signals directed Vα14i-DP thymocytes toward a transition state, characterized by absence of RORγt, CD4, and CD8, where TCR-induced immediate-early gene expression peaked and subsequently declined. Our analyses indicated that CD24-expressing iNKT cells encompassed a highly heterogenous group of cells up to 3 days after TCR expression and that Egr2 or CD69 were not optimal to further subdivide this population (Bennstein, 2018; Wang and Hogquist, 2018). TCR-induced proliferation has been assigned to stage 0 (Prevot et al., 2015; Pyaram et al., 2019; Salio et al., 2014) and stage 1 (Benlagha et al., 2002; Benlagha et al., 2005; Dose et al., 2009; Föhse et al., 2013; Wang and Hogquist, 2018) of iNKT cell development. In agreement with the latter, we found that CD24-expressing iNKT cells were largely quiescent and that the proliferative burst happened at later stages. The induction of the lineage-defining transcription factor PLZF—which went hand in hand with the acquisition of IL-4 and after a minimal delay IL-4/IFN-γ production abilities—strictly followed the loss of TCR signals.

Within 2 to 3 days after initial PLZF expression, developing iNKT cells uniformly reached a committed CD24^{-} CD44$^{-/lo}$ CD4^{+} CCR7^{+} PD-1^{+} PLZF^{hi} T-bet^{-} RORγt^{-} progenitor state characterized by vigorous proliferation that strongly resembled the NKTp cells defined by the Hogquist group (Wang and Hogquist, 2018), with the exception of high PD-1 expression in our cells.

The onset of thymic egress correlated with the time of highest proliferation in the thymus, confirming that early iNKT cells underwent robust proliferation prior thymic egress (Benlagha et al., 2002). Our window of thymic egress was also in line with the view that iNKT RTE represent mostly immature cells (Wang and Hogquist, 2018). However, the start of egress coincided with visible subset diversification, indicating that subset-primed and actively differentiating progenitors populated the periphery. Whether or not functional subset differentiation can occur independently of the thymus therefore remains an open question.

We observed the first differentiation of PLZF^{hi} progenitor cells toward the NKT1 and NKT17 fates at day 5–6. We did not detect any evidence for instructive TCR signals in PLZF-expressing iNKT cells. We therefore proposed that homogeneous TCR signals triggered a general iNKT cell fate decision during positive selection and that the complete cessation of TCR signals prior to PLZF-expression allowed subsequent effector differentiation in the absence of cytokine secretion, with the exception of IL-4. High levels of PLZF keep the progenitor cells in an activated state, permissive to effector gene expression and differentiation through repression of Bach2 and other mechanisms (Mao et al., 2016). Effector subset diversification is then driven by TCR-independent signals, yet unknown and/or previously linked to this process, including microenvironmental cytokine signals and other stimuli (Gordy et al., 2011; Havenar-Daughton et al., 2012; Miller et al., 2018; Webster et al., 2014; White et al., 2014). Our analyses of Stat5, Smad2/3, and Stat3 phosphorylation showed that PLZF^{hi} iNKT progenitor cells were in a highly cytokine stimulated, homogeneous, and therefore most likely very plastic state. Our data implied that effector lineage divergence was not driven by acute strong binary stimulation caused by absence or presence of one particular cytokine but rather by the added effects of small differences in positive and negative signals combined perhaps with stochastic events. Individually chosen fates were subsequently solidified over time, probably corresponding to downregulation of PLZF expression.

Our analyses suggested that cells identified as NKT2 in C57BL/6 mice remain similar to the NKTp cells but undergo a limited general maturation pathway shared with the other two subsets. In absence of cellular influx, mature CD44^{+} PLZF^{hi} NKT2-like cells disappeared over time, suggesting that they do not represent a stable, self-renewing population.

NKT17 cell development was proposed to occur through retention of RORγt expression in DP thymocyte precursors (Michel et al., 2008), implying an alternative pathway to differentiation from RORγt^{-} NKTp progenitors (Wang and Hogquist, 2018). Here, we provided clear kinetic evidence that NKT17 differentiation from DP thymocytes only occurred after initial decrease followed by a second wave of RORγt expression on PLZF^{hi} cells

(C) Representative FACS plots showing the percentages of thymic Vα14i-DP, NKT1, NKT2, and NKT17 cell subsets from C57BL/6 mice at the indicated ages. Numbers indicate mean ± SD.

(D) Percentage (upper graph) and absolute cell number (lower graph) of thymic Vα14i-DP, NKT1, NKT2, and NKT17 subsets isolated from C57BL/6 mice at the indicated ages. Data show mean ± SD.

Number of replicates and independent experiments is reported in Table S2.

and the subsequent acquisition of a fully functional differentiated NKT17 state within 2 to 3 days. IL-17 production capability was broadly added to the cytokine potential of the progenitor cells, as we detected IL-17-, IL-4/IL-17-, and IL-4/IFN-γ/IL-17-producing cells within the earliest NKT17 cells. The short generation window as well as subsequent cellular loss suggested that under steady-state conditions, there is a higher turnover of thymic NKT17 compared with NKT1 cells. Selected peripheral locations appeared to offer better conditions for the maintenance of NKT17 cells.

From day 6 to 10, both PLZF^{hi} RORγt^{+} and PLZF^{hi} T-bet^{+} cells underwent a parallel 4-fold increase, triggered by differentiation from PLZF^{hi} progenitor cells and ongoing proliferation. As the NKT17 subset started to contract after day 10, their production fully depended on acute differentiation from transiently available PLZF^{hi} progenitor cells and a short proliferative burst. In striking contrast, T-bet^{+} iNKT cells continued to downregulate PLZF, gradually acquired NK1.1, and continuously expanded at the expense of PLZF^{hi} cells. Therefore, NKT1 generation consisted of an initial differentiation and proliferation burst similar to NKT17 cells but, in addition, was fueled by constant differentiation from maturing PLZF^{hi}/NKT2-like cells. A terminally differentiated NKT1 state was slowly acquired over time. DN mature NKT1 cells, harboring different functions than CD4^{+} NKT1 cells (Wang and Hogquist, 2018), could arise through downregulation of CD4.

These effector subset dynamics can in principle offer an alternative or additional indirect explanation for genetic findings correlating altered TCR signal strength (Dashtsoodol et al., 2019; Wang and Hogquist, 2018) or PLZF expression (Park et al., 2019) to changes in subset differentiation. Alterations reducing *de novo* thymic iNKT cell generation rates would proportionally favor the NKT1 subset at the expense of NKT17 and even more so NKT2 cells, which are characterized by higher turnover. In essence, this would equal comparison of iNKT cell populations in younger mice with those in older mice, where there is less influx, and the steady state is dominated by the most stable population. Enhanced *de novo* generation rates would yield the opposite effect.

In summary, our developmental wave allowed us to define the precise temporal sequence of events guiding iNKT cell development. TCR signals instruct a general iNKT cell progenitor fate but not subset differentiation. NKT17 cells derive from these progenitors during a short proliferative phase within 3 to 5 days, while NKT1 cells in addition continuously emerge through differentiation from NKTp/NKT2-like cells in a process that lasts 14–20 days.

Limitations of the study

Our study was entirely conducted in mice, and its cross-validation with human NKT cell development remains a challenge. While all our analyses indicated that early iNKT cell development is highly homogeneous, future single-cell sequencing approaches could help to solidify this view. The further identification of effector subset defining cytokine and additional signals will most likely involve deep single-cell sequencing of iNKT subpopulations during earliest effector differentiation combined with comprehensive analyses of intracellular signaling. Furthermore, future studies delineating the temporal dynamics of NKT2 differentiation should be conducted in BALB/c or C57BL/6:BALB/c F1 mice.

STAR★METHODS

Detailed methods are provided in the online version of this paper and include the following:

- KEY RESOURCES TABLE
- RESOURCE AVAILABILITY
  - Lead contact
  - Materials Availability
  - Data and code availability
- EXPERIMENTAL MODELS AND SUBJECT DETAILS
  - Mice
- METHOD DETAILS
  - 4-Hydroxytamoxifen preparation
  - Administration and titration of 4-hydroxytamoxifen
  - Organ collection and single cell suspension generation
  - α-GalCer-loaded CD1d dimer preparation
  - Flow cytometry
  - RNA flow cytometry (PrimeFlow)
  - Phosflow and endogenous Nur77 staining
  - *In vivo* Bromodeoxyuridine (BrdU) assay
  - *Ex vivo* cytokine stimulation
  - iNKT cell enrichment
  - Cell sorting
  - 3′ RNA-sequencing
  - 3′ RNA-sequencing data analysis
  - Mathematical estimation of the TCR-stimulus length
- QUANTIFICATION AND STATISTICAL ANALYSIS

SUPPLEMENTAL INFORMATION

Supplemental information can be found online at https://doi.org/10.1016/j.immuni.2021.09.003.

ACKNOWLEDGMENTS

This work was supported by the DFG through CRC1054, project A02 to M.S.S. We thank J. Knogler, M. Mittermeier, L. Zaygerman, and M. Utzt for technical help as well as T. Korn and L. Klein for advice. We thank Derek Sant'Angelo for PLZFeGFP mice and the NIH Tetramer Core facility for mCD1d-PBS57 Tetramers.

AUTHOR CONTRIBUTIONS

Conceptualization, M.S.-S. and S.B.; investigation, S.B., N.D., C.D., S.H., T.A., and R.Ö.; formal analysis, S.B., T.E., J.M., A.T., M.F., M.S., M.C.-T., B.K., M.O., and M.S.-S.; writing – original draft, review & editing, S.B., N.D., and M.S.S.; funding acquisition, M.S.S.; resources, T.B. and M.O.; supervision, M.S.S. and R.R.

DECLARATION OF INTERESTS

The authors declare no competing interests.

Received: July 27, 2020
Revised: September 14, 2020
Accepted: September 2, 2021
Published: September 24, 2021

REFERENCES

Allende, M.L., Zhou, D., Kalkofen, D.N., Benhamed, S., Tuymetova, G., Borowski, C., Bendelac, A., and Proia, R.L. (2008). S1P1 receptor expression regulates emergence of NKT cells in peripheral tissues. FASEB J. *22*, 307–315.

Alonzo, E.S., Gottschalk, R.A., Das, J., Egawa, T., Hobbs, R.M., Pandolfi, P.P., Pereira, P., Nichols, K.E., Koretzky, G.A., Jordan, M.S., and Sant'Angelo, D.B. (2010). Development of promyelocytic zinc finger and ThPOK-expressing innate gamma delta T cells is controlled by strength of TCR signaling and Id3. J. Immunol. *184*, 1268–1279.

Bendelac, A., Savage, P.B., and Teyton, L. (2007). The biology of NKT cells. Annu. Rev. Immunol. *25*, 297–336.

Bending, D., Prieto Martín, P., Paduraru, A., Ducker, C., Marzaganov, E., Laviron, M., Kitano, S., Miyachi, H., Crompton, T., and Ono, M. (2018). A timer for analyzing temporally dynamic changes in transcription during differentiation in vivo. J. Cell Biol. *217*, 2931–2950.

Benlagha, K., Kyin, T., Beavis, A., Teyton, L., and Bendelac, A. (2002). A thymic precursor to the NK T cell lineage. Science *296*, 553–555.

Benlagha, K., Wei, D.G., Veiga, J., Teyton, L., and Bendelac, A. (2005). Characterization of the early stages of thymic NKT cell development. J. Exp. Med. *202*, 485–492.

Bennstein, S.B. (2018). Unraveling Natural Killer T-Cells Development. Front. Immunol. *8*, 1950.

Blume, J., Zur Lage, S., Witzlau, K., Georgiev, H., Weiss, S., Łyszkiewicz, M., Ziętara, N., and Krueger, A. (2016). Overexpression of Vα14Jα18 TCR promotes development of iNKT cells in the absence of miR-181a/b-1. Immunol. Cell Biol. *94*, 741–746.

Borg, N.A., Wun, K.S., Kjer-Nielsen, L., Wilce, M.C., Pellicci, D.G., Koh, R., Besra, G.S., Bharadwaj, M., Godfrey, D.I., McCluskey, J., and Rossjohn, J. (2007). CD1d-lipid-antigen recognition by the semi-invariant NKT T-cell receptor. Nature *448*, 44–49.

Chen, E.Y., Tan, C.M., Kou, Y., Duan, Q., Wang, Z., Meirelles, G.V., Clark, N.R., and Ma'ayan, A. (2013). Enrichr: interactive and collaborative HTML5 gene list enrichment analysis tool. BMC Bioinformatics *14*, 128.

Chen, S., Cai, C., Li, Z., Liu, G., Wang, Y., Blonska, M., Li, D., Du, J., Lin, X., Yang, M., and Dong, Z. (2017). Dissection of SAP-dependent and SAP-independent SLAM family signaling in NKT cell development and humoral immunity. J. Exp. Med. *214*, 475–489.

Cui, J., Shin, T., Kawano, T., Sato, H., Kondo, E., Toura, I., Kaneko, Y., Koseki, H., Kanno, M., and Taniguchi, M. (1997). Requirement for Valpha14 NKT cells in IL-12-mediated rejection of tumors. Science *278*, 1623–1626.

Cui, G., Hara, T., Simmons, S., Wagatsuma, K., Abe, A., Miyachi, H., Kitano, S., Ishii, M., Tani-ichi, S., and Ikuta, K. (2014). Characterization of the IL-15 niche in primary and secondary lymphoid organs in vivo. Proc. Natl. Acad. Sci. USA *111*, 1915–1920.

Dashtsoodol, N., Shigeura, T., Ozawa, R., Harada, M., Kojo, S., Watanabe, T., Koseki, H., Nakayama, M., Ohara, O., and Taniguchi, M. (2016). Generation of Novel Traj18-Deficient Mice Lacking Vα14 Natural Killer T Cells with an Undisturbed T Cell Receptor α-Chain Repertoire. PLoS ONE *11*, e0153347.

Dashtsoodol, N., Bortoluzzi, S., and Schmidt-Supprian, M. (2019). T Cell Receptor Expression Timing and Signal Strength in the Functional Differentiation of Invariant Natural Killer T Cells. Front. Immunol. *10*, 841.

Dose, M., Sleckman, B.P., Han, J., Bredemeyer, A.L., Bendelac, A., and Gounari, F. (2009). Intrathymic proliferation wave essential for Valpha14+ natural killer T cell development depends on c-Myc. Proc. Natl. Acad. Sci. USA *106*, 8641–8646.

Drees, C., Vahl, J.C., Bortoluzzi, S., Heger, K.D., Fischer, J.C., Wunderlich, F.T., Peschel, C., and Schmidt-Supprian, M. (2017). Roquin Paralogs Differentially Regulate Functional NKT Cell Subsets. J. Immunol. *198*, 2747–2759.

Engel, I., Seumois, G., Chavez, L., Samaniego-Castruita, D., White, B., Chawla, A., Mock, D., Vijayanand, P., and Kronenberg, M. (2016). Innate-like functions of natural killer T cell subsets result from highly divergent gene programs. Nat. Immunol. *17*, 728–739.

Föhse, L., Reinhardt, A., Oberdörfer, L., Schmitz, S., Förster, R., Malissen, B., and Prinz, I. (2013). Differential postselection proliferation dynamics of αβ T cells, Foxp3+ regulatory T cells, and invariant NKT cells monitored by genetic pulse labeling. J. Immunol. *191*, 2384–2392.

Gleimer, M., von Boehmer, H., and Kreslavsky, T. (2012). PLZF Controls the Expression of a Limited Number of Genes Essential for NKT Cell Function. Front. Immunol. *3*, 374.

Godfrey, D.I., Uldrich, A.P., McCluskey, J., Rossjohn, J., and Moody, D.B. (2015). The burgeoning family of unconventional T cells. Nat. Immunol. *16*, 1114–1123.

Gordy, L.E., Bezbradica, J.S., Flyak, A.I., Spencer, C.T., Dunkle, A., Sun, J., Stanic, A.K., Boothby, M.R., He, Y.W., Zhao, Z., et al. (2011). IL-15 regulates homeostasis and terminal maturation of NKT cells. J. Immunol. *187*, 6335–6345.

Griewank, K., Borowski, C., Rietdijk, S., Wang, N., Julien, A., Wei, D.G., Mamchak, A.A., Terhorst, C., and Bendelac, A. (2007). Homotypic interactions mediated by Slamf1 and Slamf6 receptors control NKT cell lineage development. Immunity *27*, 751–762.

Hänzelmann, S., Castelo, R., and Guinney, J. (2013). GSVA: gene set variation analysis for microarray and RNA-seq data. BMC Bioinformatics *14*, 7.

Havenar-Daughton, C., Li, S., Benlagha, K., and Marie, J.C. (2012). Development and function of murine RORγt+ iNKT cells are under TGF-β signaling control. Blood *119*, 3486–3494.

Henao-Mejia, J., Williams, A., Goff, L.A., Staron, M., Licona-Limón, P., Kaech, S.M., Nakayama, M., Rinn, J.L., and Flavell, R.A. (2013). The microRNA miR-181 is a critical cellular metabolic rheostat essential for NKT cell ontogenesis and lymphocyte development and homeostasis. Immunity *38*, 984–997.

Heng, T.S., and Painter, M.W.; Immunological Genome Project Consortium (2008). The Immunological Genome Project: networks of gene expression in immune cells. Nat. Immunol. *9*, 1091–1094.

Hogquist, K., and Georgiev, H. (2020). Recent advances in iNKT cell development. F1000Res. *9*.

Kovalovsky, D., Uche, O.U., Eladad, S., Hobbs, R.M., Yi, W., Alonzo, E., Chua, K., Eidson, M., Kim, H.J., Im, J.S., et al. (2008). The BTB-zinc finger transcriptional regulator PLZF controls the development of invariant natural killer T cell effector functions. Nat. Immunol. *9*, 1055–1064.

Kretschmer, L., Flossdorf, M., Mir, J., Cho, Y.L., Plambeck, M., Treise, I., Toska, A., Heinzel, S., Schiemann, M., Busch, D.H., and Buchholz, V.R. (2020). Differential expansion of T central memory precursor and effector subsets is regulated by division speed. Nat. Commun. *11*, 113.

Kronenberg, M. (2005). Toward an understanding of NKT cell biology: progress and paradoxes. Annu. Rev. Immunol. *23*, 877–900.

Kuleshov, M.V., Jones, M.R., Rouillard, A.D., Fernandez, N.F., Duan, Q., Wang, Z., Koplev, S., Jenkins, S.L., Jagodnik, K.M., Lachmann, A., et al. (2016). Enrichr: a comprehensive gene set enrichment analysis web server 2016 update. Nucleic Acids Res. *44*, W90–W97.

Lee, Y.J., Holzapfel, K.L., Zhu, J., Jameson, S.C., and Hogquist, K.A. (2013). Steady-state production of IL-4 modulates immunity in mouse strains and is determined by lineage diversity of iNKT cells. Nat. Immunol. *14*, 1146–1154.

Lee, Y.J., Starrett, G.J., Lee, S.T., Yang, R., Henzler, C.M., Jameson, S.C., and Hogquist, K.A. (2016). Lineage-Specific Effector Signatures of Invariant NKT Cells Are Shared amongst γδ T, Innate Lymphoid, and Th Cells. J. Immunol. *197*, 1460–1470.

Liberzon, A., Subramanian, A., Pinchback, R., Thorvaldsdóttir, H., Tamayo, P., and Mesirov, J.P. (2011). Molecular signatures database (MSigDB) 3.0. Bioinformatics *27*, 1739–1740.

Love, M.I., Huber, W., and Anders, S. (2014). Moderated estimation of fold change and dispersion for RNA-seq data with DESeq2. Genome Biol. *15*, 550.

Lu, Y., Zhong, M.C., Qian, J., Calderon, V., Cruz Tleugabulova, M., Mallevaey, T., and Veillette, A. (2019). SLAM receptors foster iNKT cell development by reducing TCR signal strength after positive selection. Nat. Immunol. *20*, 447–457.

Ma, C.Y., Marioni, J.C., Griffiths, G.M., and Richard, A.C. (2020). Stimulation strength controls the rate of initiation but not the molecular organisation of TCR-induced signalling. eLife *9*, e53948.

Macosko, E.Z., Basu, A., Satija, R., Nemesh, J., Shekhar, K., Goldman, M., Tirosh, I., Bialas, A.R., Kamitaki, N., Martersteck, E.M., et al. (2015). Highly Parallel Genome-wide Expression Profiling of Individual Cells Using Nanoliter Droplets. Cell *161*, 1202–1214.

Madisen, L., Zwingman, T.A., Sunkin, S.M., Oh, S.W., Zariwala, H.A., Gu, H., Ng, L.L., Palmiter, R.D., Hawrylycz, M.J., Jones, A.R., et al. (2010). A robust and high-throughput Cre reporting and characterization system for the whole mouse brain. Nat. Neurosci. *13*, 133–140.

Malhotra, N., Qi, Y., Spidale, N.A., Frascoli, M., Miu, B., Cho, O., Sylvia, K., and Kang, J. (2018). SOX4 controls invariant NKT cell differentiation by tuning TCR signaling. J. Exp. Med. *215*, 2887–2900.

Mao, A.P., Constantinides, M.G., Mathew, R., Zuo, Z., Chen, X., Weirauch, M.T., and Bendelac, A. (2016). Multiple layers of transcriptional regulation by PLZF in NKT-cell development. Proc. Natl. Acad. Sci. USA *113*, 7602–7607.

Matsuda, J.L., Gapin, L., Sidobre, S., Kieper, W.C., Tan, J.T., Ceredig, R., Surh, C.D., and Kronenberg, M. (2002). Homeostasis of V alpha 14i NKT cells. Nat. Immunol. *3*, 966–974.

Michel, M.L., Mendes-da-Cruz, D., Keller, A.C., Lochner, M., Schneider, E., Dy, M., Eberl, G., and Leite-de-Moraes, M.C. (2008). Critical role of ROR-γt in a new thymic pathway leading to IL-17-producing invariant NKT cell differentiation. Proc. Natl. Acad. Sci. USA *105*, 19845–19850.

Miller, C.N., Proekt, I., von Moltke, J., Wells, K.L., Rajpurkar, A.R., Wang, H., Rattay, K., Khan, I.S., Metzger, T.C., Pollack, J.L., et al. (2018). Thymic tuft cells promote an IL-4-enriched medulla and shape thymocyte development. Nature *559*, 627–631.

Pandiyan, P., Yang, X.P., Saravanamuthu, S.S., Zheng, L., Ishihara, S., O'Shea, J.J., and Lenardo, M.J. (2012). The role of IL-15 in activating STAT5 and fine-tuning IL-17A production in CD4 T lymphocytes. J. Immunol. *189*, 4237–4246.

Parekh, S., Ziegenhain, C., Vieth, B., Enard, W., and Hellmann, I. (2016). The impact of amplification on differential expression analyses by RNA-seq. Sci. Rep. *6*, 25533.

Park, J.Y., DiPalma, D.T., Kwon, J., Fink, J., and Park, J.H. (2019). Quantitative Difference in PLZF Protein Expression Determines iNKT Lineage Fate and Controls Innate CD8 T Cell Generation. Cell Rep. *27*, 2548–2557.

Pereira, R.M., Martinez, G.J., Engel, I., Cruz-Guilloty, F., Barboza, B.A., Tsagaratou, A., Lio, C.W., Berg, L.J., Lee, Y., Kronenberg, M., et al. (2014). Jarid2 is induced by TCR signalling and controls iNKT cell maturation. Nat. Commun. *5*, 4540.

Prevot, N., Pyaram, K., Bischoff, E., Sen, J.M., Powell, J.D., and Chang, C.H. (2015). Mammalian target of rapamycin complex 2 regulates invariant NKT cell development and function independent of promyelocytic leukemia zinc-finger. J. Immunol. *194*, 223–230.

Pyaram, K., Kumar, A., Kim, Y.H., Noel, S., Reddy, S.P., Rabb, H., and Chang, C.H. (2019). Keap1-Nrf2 System Plays an Important Role in Invariant Natural Killer T Cell Development and Homeostasis. Cell Rep. *27*, 699–707.

Roederer, M., Nozzi, J.L., and Nason, M.C. (2011). SPICE: exploration and analysis of post-cytometric complex multivariate datasets. Cytometry A. *79*, 167–174.

Salio, M., Puleston, D.J., Mathan, T.S., Shepherd, D., Stranks, A.J., Adamopoulou, E., Veerapen, N., Besra, G.S., Hollander, G.A., Simon, A.K., and Cerundolo, V. (2014). Essential role for autophagy during invariant NKT cell development. Proc. Natl. Acad. Sci. USA *111*, E5678–E5687.

Savage, A.K., Constantinides, M.G., Han, J., Picard, D., Martin, E., Li, B., Lantz, O., and Bendelac, A. (2008). The transcription factor PLZF directs the effector program of the NKT cell lineage. Immunity *29*, 391–403.

Sledzińska, A., Hemmers, S., Mair, F., Gorka, O., Ruland, J., Fairbairn, L., Nissler, A., Müller, W., Waisman, A., Becher, B., and Buch, T. (2013). TGF-β signalling is required for $CD4^+$ T cell homeostasis but dispensable for regulatory T cell function. PLoS Biol. *11*, e1001674.

St Leger, A.J., Hansen, A.M., Karauzum, H., Horai, R., Yu, C.R., Laurence, A., Mayer-Barber, K.D., Silver, P., Villasmil, R., Egwuagu, C., et al. (2018). STAT-3-independent production of IL-17 by mouse innate-like αβ T cells controls ocular infection. J. Exp. Med. *215*, 1079–1090.

Subramanian, A., Tamayo, P., Mootha, V.K., Mukherjee, S., Ebert, B.L., Gillette, M.A., Paulovich, A., Pomeroy, S.L., Golub, T.R., Lander, E.S., and Mesirov, J.P. (2005). Gene set enrichment analysis: a knowledge-based approach for interpreting genome-wide expression profiles. Proc. Natl. Acad. Sci. USA *102*, 15545–15550.

Taniguchi, M., Harada, M., Kojo, S., Nakayama, T., and Wakao, H. (2003). The regulatory role of Valpha14 NKT cells in innate and acquired immune response. Annu. Rev. Immunol. *21*, 483–513.

Tuttle, K.D., Krovi, S.H., Zhang, J., Bedel, R., Harmacek, L., Peterson, L.K., Dragone, L.L., Lefferts, A., Halluszczak, C., Riemondy, K., et al. (2018). TCR signal strength controls thymic differentiation of iNKT cell subsets. Nat. Commun. *9*, 2650.

Vahl, J.C., Heger, K., Knies, N., Hein, M.Y., Boon, L., Yagita, H., Polic, B., and Schmidt-Supprian, M. (2013). NKT cell-TCR expression activates conventional T cells in vivo, but is largely dispensable for mature NKT cell biology. PLoS Biol. *11*, e1001589.

Wang, H., and Hogquist, K.A. (2018). CCR7 defines a precursor for murine iNKT cells in thymus and periphery. eLife *7*, e34793.

Webster, K.E., Kim, H.O., Kyparissoudis, K., Corpuz, T.M., Pinget, G.V., Uldrich, A.P., Brink, R., Belz, G.T., Cho, J.H., Godfrey, D.I., and Sprent, J. (2014). IL-17-producing NKT cells depend exclusively on IL-7 for homeostasis and survival. Mucosal Immunol. *7*, 1058–1067.

White, A.J., Jenkinson, W.E., Cowan, J.E., Parnell, S.M., Bacon, A., Jones, N.D., Jenkinson, E.J., and Anderson, G. (2014). An essential role for medullary thymic epithelial cells during the intrathymic development of invariant NKT cells. J. Immunol. *192*, 2659–2666.

Wickham, H. (2016). ggplot2: Elegant Graphics for Data Analysis (New York: Springer-Verlag).

Wilson, R.P., Ives, M.L., Rao, G., Lau, A., Payne, K., Kobayashi, M., Arkwright, P.D., Peake, J., Wong, M., Adelstein, S., et al. (2015). STAT3 is a critical cell-intrinsic regulator of human unconventional T cell numbers and function. J. Exp. Med. *212*, 855–864.

Zhao, M., Svensson, M.N.D., Venken, K., Chawla, A., Liang, S., Engel, I., Mydel, P., Day, J., Elewaut, D., Bottini, N., and Kronenberg, M. (2018). Altered thymic differentiation and modulation of arthritis by invariant NKT cells expressing mutant ZAP70. Nat. Commun. *9*, 2627.

Zhu, L., Qiao, Y., Choi, E.S., Das, J., Sant'angelo, D.B., and Chang, C.H. (2013). A transgenic TCR directs the development of IL-4+ and PLZF+ innate CD4 T cells. J. Immunol. *191*, 737–744.

Zikherman, J., Parameswaran, R., and Weiss, A. (2012). Endogenous antigen tunes the responsiveness of naive B cells but not T cells. Nature *489*, 160–164.

STAR★METHODS

KEY RESOURCES TABLE

REAGENT or RESOURCE	SOURCE	IDENTIFIER
Antibodies		
Anti-BrdU FITC	BioLegend	Cat#: 364104; RRID: AB_2564481
Anti-mouse CD3ε PE/Cy7	BioLegend	Cat#: 100320; RRID: AB_312685
Anti-mouse CD3ε Biotin	BD	Cat#: 553059; RRID: AB_394592
Anti-mouse CD4 APC-Cy7	BioLegend	Cat#: 100525; RRID: AB_312726
Anti-mouse CD4 BV605	BioLegend	Cat#: 100451; RRID: AB_2564591
Anti-mouse CD4 PE	eBioscience	Cat#: 12-0042-83; RRID: AB_465511
Anti-mouse CD4 PE/Cy5	BioLegend	Cat#: 100410; RRID: AB_312695
Anti-mouse CD8a APCeF780	eBioscience	Cat#: 47-0081-82; RRID: AB_1272185
Anti-mouse CD8a BV605	BioLegend	Cat#: 100743; RRID: AB_2561352
Anti-rat/mouse CD8a BUV395	BD	Cat#: 565968; RRID: AB_2739421
Anti-rat/mouse CD8a BUV737	BD	Cat#: 612759; RRID: AB_2870090
Anti-mouse CD8a FITC	eBioscience	Cat#: 11-0081-85; RRID: AB_464916
Anti-mouse CD8a PerCPeF710	eBioscience	Cat#: 46-0081-82; RRID: AB_1834433
Anti-mouse CD16/CD32	eBioscience	Cat#: 14-0161-86; RRID: AB_467135
Anti-mouse CD19 AF700	eBioscience	Cat#: 56-0193-82; RRID: AB_837083
Anti-mouse CD24 FITC	eBioscience	Cat#: 11-0242-82; RRID: AB_464988
Anti-mouse CD24 PE/Cy7	eBioscience	Cat#: 25-0242-82; RRID: AB_10853806
Anti-human/mouse/rat CD27 APCeF780	eBioscience	Cat#: 47-0271-82; RRID: AB_10853642
Anti-human/mouse CD44 AF700	BioLegend	Cat#: 103026; RRID: AB_493713
Anti-human/mouse CD44 PE/Cy7	eBioscience	Cat#: 25-0441-82; RRID: AB_469623
Anti-mouse CD69 PE/Cy7	eBioscience	Cat#: 25-0691-82; RRID: AB_469637
Anti-mouse CD103 BV510	BioLegend	Cat#: 121423; RRID:AB_2562713
Anti-mouse CD138 BV421	BioLegend	Cat#: 142508; RRID: AB_11203544
Anti-mouse CD197 (CCR7) BV421	BD	Cat#: 566291; RRID: AB_2737001
Anti-mouse CD197 (CCR7) PE	eBioscience	Cat#: 12-1971-82; RRID: AB_465905
Anti-mouse CD278 (ICOS) Biotin	eBioscience	Cat#: 13-9942-81; RRID: AB_467001
Anti-human/mouse/rat CD278 (ICOS) BV421	BioLegend	Cat#: 313523; RRID: AB_2562538
Anti-mouse CD279 (PD-1) PE/Cy7	eBioscience	Cat#: 25-9985-82; RRID: AB_10853805
Anti-mouse Egr2 PE	eBioscience	Cat#: 12-6691-82; RRID: AB_10717804
Anti-mouse/rat Foxp3 PE	eBioscience	Cat#: 12-5773-82; RRID: AB_465936
Anti-human/mouse GATA3 PE	eBioscience	Cat#: 12-9966-42; RRID: AB_1963600
Anti-human/mouse GATA3 PE-CF594	BD	Cat#: 563510; RRID: AB_2738248
Anti-human/mouse GATA3 PerCPeF710	eBioscience	Cat#: 46-9966-42; RRID: AB_10804487
Rat anti-mouse IgG1 APC	BD	Cat#: 550874; RRID: AB_398470
Anti-mouse IL-4 BV421	BioLegend	Cat#: 504119; RRID: AB_10896945
Anti-mouse IL-17A BV605	BD	Cat#: 564169; RRID: AB_2738640
Anti-IL-17RB PE	BioLegend	Cat#: 146305; RRID: AB_2564511
Anti-mouse IL-23R BV421	BioLegend	Cat#: 150907; RRID: AB_2715804
Anti-mouse IFN-γ PE/Cy7	eBioscience	Cat#: 25-7311-82; RRID: AB_469680
Anti-human/mouse Ki67 PerCPeF710	eBioscience	Cat#: 46-5698-80; RRID: AB_11039489
Anti-mouse CD304 (Neuropilin-1) BV421	BioLegend	Cat#: 145209; RRID: AB_2562358
Anti-mouse NK1.1 BV421	BioLegend	Cat#: 108741; RRID: AB_2562561
Anti-mouse NK1.1 BV650	BioLegend	Cat#: 108736; RRID: AB_2563159
Anti-mouse NK1.1 BUV395	BD	Cat#: 564144; RRID: AB_2738618

(*Continued on next page*)

Continued

REAGENT or RESOURCE	SOURCE	IDENTIFIER
Anti-mouse NK1.1 BUV737	BD	Cat#: 741715; RRID: AB_2871088
Anti-mouse NK1.1 PE	eBioscience	Cat#: 12-5941-82; RRID: AB_466050
Anti-mouse NK1.1 PE/Cy7	eBioscience	Cat#: 25-5941-81; RRID: AB_469664
Anti-mouse Nur77 PE	eBioscience	Cat#: 12-5965-82; RRID: AB_1257209
Anti-human/mouse PLZF AF488	eBioscience	Cat#: 53-9320-82; RRID: AB_2574445
Anti-mouse PLZF PE	BioLegend	Cat#: 145803; RRID: AB_2561973
Anti-mouse PLZF PE/Cy7	BioLegend	Cat#: 145806; RRID: AB_2566164
Anti-mouse RORγt BV421	BD	Cat#: 562894; RRID: AB_2687545
Anti-mouse RORγt PEeF610	eBioscience	Cat#: 61-6981-82; RRID: AB_2574650
Anti-mouse RORγt PerCPeF710	eBioscience	Cat#: 46-6981-82; RRID: AB_10717956
Anti-mouse $S1P_1$/EDG-1	R&D	Cat#: MAB7089; RRID: AB_10994183
Anti-mouse S6 (pS235/pS236) V450	BD	Cat#: 561457; RRID: AB_10643763
Anti-mouse Smad2 (pS465/pS467)/Smad3 (pS423/pS425) PE-CF594	BD	Cat#: 56269; RRID: AB_2737728
Anti-mouse Stat3 (pS727) PE	BD	Cat#: 558557; RRID: AB_647232
Anti-mouse Stat5 (pY694) PE	BD	Cat#: 612567; RRID: AB_399858
Anti-mouse Stat5 (pY694) AF488	BD	Cat#: 562075; RRID: AB_11154039
Anti-Streptavidin PerCP-Cy5.5	eBioscience	Cat#: 45-4317-82; RRID: AB_10311495
Anti-Streptavidin BV650	BioLegend	Cat#: 405231; RRID: N/A
Anti-human/mouse T-bet BV605	BioLegend	Cat#: 644817; RRID: AB_11219388
Anti-human/mouse T-bet PE/Cy7	eBioscience	Cat#: 25-5825-82; RRID: AB_11042699
Anti-mouse TCRβ BV510	BioLegend	Cat#: 109234; RRID: AB_2562350
Anti-mouse TCRβ BV605	BD	Cat#: 562840; RRID: AB_2687544
Anti-mouse ThPOK PE	eBioscience	Cat#: 12-5928-82; RRID: AB_11149862
Donkey Anti-Rat IgG (H+L) FITC	Thermo Fisher	Cat#: A18746; RRID: AB_2535523
mCD1d-PBS57 APC	NIH Tetramer Core facility	Cat#: N/A; RRID: N/A
Purified Mouse IgG1 λ Isotype Control	BD	Cat#: 553485; RRID: AB_479649
Chemicals, peptides, and recombinant proteins		
2-mercaptoethanol	GIBCO	Cat#: 31350-010
2-mercaptoethanol	Merck	Cat#: 8.05740-0250
4-Hydroxytamoxifen	Sigma-Aldrich	Cat#: H6278-50MG
α-Galactosylceramide	Funakoshi	Cat#: KRN7000
7-Aminoactinomycin D (7-AAD)	Thermo Fisher	Cat#: 00-6993-50
Bromodeoxyuridine (BrdU)	BioLegend	Cat#: 423401
BSA	Carl-Roth	Cat#: 0163.4
Corn oil	Sigma-Aldrich	Cat#: C8267-500ML
Deoxyribonuclease I from bovine pancreas	Sigma-Aldrich	Cat#: D4263-5VL
DimerX I	BD	Cat#: 557599
DRAQ5 (5mM)	Abcam	Cat#: ab108410
EDTA, 0.5M	Promega	Cat#: 0000142515
Easycoll separating solution	Biochrom	Cat#: L 6145
Fetal Bovine Serum (FBS)	GIBCO	Cat#: 10270-106
Heparin	Sigma-Aldrich	Cat#: 9041-08-1
HEPES, 1M	GIBCO	Cat#: 15630-056
Ionomycin	Merck Millipore	Cat#: 407953
L-Glutamine	GIBCO	Cat#: 25030-081
LIVE/DEAD™ Fixable Near-IR Dead Cell Stain Kit	Invitrogen	Cat#: L10119
Maxima H Minus Reverse Transcriptase	Thermo Fisher	Cat#: EP0751
Monensin 1000x	eBioscience	Cat#: 00-4505-51

(*Continued on next page*)

Continued

REAGENT or RESOURCE	SOURCE	IDENTIFIER
Non-essential amino acids (NEAA)	Invitrogen	Cat#: L10119
Penicillin-Streptomycin	GIBCO	Cat#: 15140122
Percoll PLUS	GE Healthcare	Cat#: 17-5445-01
Phorbol 12-myristate 13-acetate (PMA)	Sigma-Aldrich	Cat#: P8139-1MG
PromoFluor-840, NIR maleimide	BioConnect	Cat#: PK-PF840-3-01
Roti®-Histofix 4%	Carl-Roth	Cat#: P087.4
RPMI medium 1640	GIBCO	Cat#: 21875-034
RT-Buffer, 5x	Thermo Fisher	Cat#: EP0752
Sodium pyruvate	GIBCO	Cat#: 11360-039
Tamoxifen	Sigma-Aldrich	Cat#: T5648-1G
TCL Buffer, 2x	QIAGEN	Cat#: 1070498
Zombie UV™ Fixable Viability Kit	BioLegend	Cat#: 423108
Critical commercial assays		
Agencourt AMPure XP	Beckman Coulter	Cat#: A63880
Anti-APC MicroBeads	Miltenyi Biotec	Cat#: 130-090-855
BD Pharmingen™ BrdU Flow Kits	BD	Cat#: 559619
BD Pharmingen™ Transcription Factor Phospho (TFP) Buffer Set	BD	Cat#: 563239
eBioscience™ Foxp3 / Transcription Factor Staining Buffer Set	eBioscience	Cat#: 00-5523-00
Nextera XT DNA Library Preparation Kit	Illumina	Cat#: FC-131-1096
PrimeFlow™ RNA Assay Kit	Thermo Fisher	Cat#: 88-18005-210
Zymoresearch DNA Clean & Concentrator™	Zymo Research	Cat#: D4004
Deposited data		
Raw data files for RNA sequencing	This paper	ENA: PRJEB46388
Experimental models: Organisms/strains		
Mouse: Cd4$^{tm1(cre/ERT2)Thbu}$ (CD4-CreER^{t2})	(Sledzińska et al., 2013)	N/A
Mouse: Tcra^{tm1Mass} (Vα14i^{StopF})	(Vahl et al., 2013)	N/A
Mouse: J$_{\alpha}$281$^{-/-}$ (Jα18$^{-/-}$)	(Cui et al., 1997)	N/A
Mouse: Traj18$^{tm1.2Tgi}$ (Trαj18$^{-/-}$)	(Dashtsoodol et al., 2016)	N/A
Mouse: B6.Cg-Gt(ROSA)26Sor$^{tm9(CAG-tdTomato)Hze}$/J (tdTomato)	(Madisen et al., 2010)	JAX: 007909
Mouse: B6.FVB(Cg)-Tg(Nr4a1-EGFP)$^{GY139Gsat/WeisMmucd}$ (Nur77eGFP)	(Zikherman et al., 2012)	MMRRC: 036737-UCD
Mouse: Tg(Zbtb16-eGFP)1Sant (PLZFeGFP)	(Zhu et al., 2013)	N/A
Mouse: Nr4a3$^{tm1.1Mono}$ (*Nr4a3*-Tocky)	(Bending et al., 2018)	N/A
Oligonucleotides		
E5V6NEXT: 5'-iCiGiCACACTCTTTCCCTACACGACGC rGrGrG-3'	Integrated DNA Technologies IDT	N/A
P5-Nextera: AATGATACGGCGACCACCGAGATCTACA CTCGTCGGCAGCGTC	Integrated DNA Technologies IDT	N/A
P7-TrueSeqP5: CAAGCAGAAGACGGCATACGAGATAC ACTCTTTCCCTACACGACGCTCTTCCGATCT	Integrated DNA Technologies IDT	N/A
SINGV6: 5'-/5Biosg/ACACTCTTTCCCTACACGACGC-3'	Integrated DNA Technologies IDT	N/A
Software and algorithms		
GraphPad Prism v7	GraphPad Software	https://www.graphpad.com
FlowJo v10	FlowJo	https://www.flowjo.com
SPICE v6	(Roederer et al., 2011)	https://niaid.github.io/spice/
Venn Diagrams	Van de Peer Lab – Bioinformatics and Evolutionary Genomics	http://bioinformatics.psb.ugent.be/webtools/Venn/

(*Continued on next page*)

Continued

REAGENT or RESOURCE	SOURCE	IDENTIFIER
R (v3.4.4 and v3.6.3)	The R Foundation	https://www.r-project.org
EnrichR	(Chen et al., 2013; Kuleshov et al., 2016)	https://maayanlab.cloud/Enrichr/
Drop-seq v1.12	(Macosko et al., 2015)	https://github.com/broadinstitute/Drop-seq/releases
Gene annotation Release M18 (GRCm38.p6) and Genome sequence	Gencode Consortium	https://www.gencodegenes.org/mouse/release_M18.html
DESeq2 v1.30.1	Bioconductor (Love et al., 2014)	DOI: 10.18129/B9.bioc.DESeq2
GSVA v1.38.2	Bioconductor (Hänzelmann et al., 2013)	DOI: 10.18129/B9.bioc.GSVA
MsigDB v7.4	UC San Diego and Broad Institute (Liberzon et al., 2011; Subramanian et al., 2005)	https://www.gsea-msigdb.org/gsea/msigdb
Other		
Anti-mouse Nfatc1 AF568 PrimeFlow Probe	Thermo Fisher	Assay ID VB10-3284056-PF, Cat#: PF-204
Anti-mouse Nr4a1 AF568 PrimeFlow Probe	Thermo Fisher	Assay ID VB10-3283147-PF, Cat#: PF-204

RESOURCE AVAILABILITY

Lead contact

Further information and requests for resources and reagents should be directed to and will be fulfilled by the Lead Contact, Marc Schmidt-Supprian (marc.supprian@tum.de).

Materials Availability

This study did not generate new unique reagents.

Data and code availability

RNA-sequencing data were deposited at ENA and are publicly available as of the date of publication. Accession number is listed in the key resources table. Processed RNA-sequencing data, including normalized gene counts and lists of differentially expressed genes, are available in the Supplementary Information (Table S3 and S6). Any additional information required to reanalyze the data reported in this paper is available from the lead contact upon request.

EXPERIMENTAL MODELS AND SUBJECT DETAILS

Mice

B6.Cg-Gt(ROSA)$^{26Sortm9(CAG-tdTomato)Hze}$/J (tdTomato) mice were purchased from The Jackson Laboratory. Sperm from B6.FVB(Cg)-Tg(Nr4a1-EGFP)$^{GY139Gsat/WeisMmucd}$ (Nur77eGFP) was purchased from the MMRRC and live mice were reconstituted at Charles River. Cd4$^{tm1(cre/ERT2)Thbu}$ (CD4-CreER^{t2}) mice, Nr4a3$^{tm1.1Mono}$ (*Nr4a3*-Tocky) mice and Tcra^{tm1Mass} (Vα14i^{StopF}) mice were provided by the authors (T.B., M.O. and M.S.S., respectively). Tg(Zbtb16-eGFP)1Sant (PLZFeGFP) mice were obtained from Derek Sant'Angelo (Rutgers University) and $J_{\alpha}281^{-/-}$ (Jα18$^{-/-}$) and Traj18$^{tm1.2Tgi}$ (Trαj18$^{-/-}$) mice were provided by Masaru Taniguchi (RIKEN).

All the mice used in this project were female and male, 6-14 weeks old, housed in a specific pathogen-free (SPF) or specific and opportunistic pathogen free (SOPF) condition, according to the legislation of the European Union and the Region of Upper Bavaria. Mice were bred and housed in mouse facilities in Charles River Calco (Italy) and in the Centre for Preclinical Research of the MRI (Zentrum für Präklinisches Forschung (ZPF), Munich). All the mouse strains used in this project are published and were generated on or later backcrossed to a C57BL/6 genetic background.

For this project, we generated CD4-CreER^{t2} Vα14i^{StopF} mice to induce iNKT cell generation. We initially further added Jα18$^{-/-}$ alleles, which were later substituted with Trαj18$^{-/-}$ alleles to abrogate the generation of endogenous iNKT cells. For the purpose of this project, these two mouse models behave similarly and are therefore combined under the name Traj18^{KO}.

To investigate late thymic iNKT cell differentiation and iNKT cell colonization of peripheral organs, we generated CD4-CreER^{t2} Vα14i^{StopF} tdTomato mice (±Traj18^{KO}). To dissect the TCR signal dynamics, we intercrossed CD4-CreER^{t2} Vα14i^{StopF} mice

(±Traj18^{KO}) with either Nur77eGFP or *Nr4a3*-Tocky mice. CD4-CreER^{t2} Vα14i^{StopF} *Nr4a3*-Tocky mice were additionally intercrossed with PLZFeGFP mice. Unless differently specified, CD4-CreER^{t2} mice were used as controls.

METHOD DETAILS

4-Hydroxytamoxifen preparation

4-Hydroxytamoxifen (4-OHT) was reconstituted and diluted at a final concentration of 3 mg/mL (for initial titration experiments, different concentrations were prepared). To prepare 1 mL of solution, 3mg of 4-OHT were collected from the original vial with an anti-static spatula and weighted on a microscale directly in a 1.5 mL safe-lock light-protected tube. Hundred microliters of 96% ethanol were added to the tube, followed by 900 μl of corn oil. The tube was then sealed and placed in a water bath sonicator for at least 30 min, or until it was completely dissolved. The tubes were then appropriately labeled and stored in a light-protected box in the freezer (−20°C). Each vial was sonicated for 10 min prior administration to the animals. During the whole preparation procedure, the appropriate Personal Protective Equipment (PPE) was used.

Administration and titration of 4-hydroxytamoxifen

In order to induce the CreER^{t2}-recombinase, one single dose of 100 μl of 4-OHT solution (corresponding to 0.3 mg of 4-OHT) was administered to the mice by oral gavage. Only for the initial titration experiments, the following concentrations were administered: 0.3 mg, 0.6 mg, 1 mg, 2 mg and 3 mg (Table S1). Unless differently specified, 4-OHT was administered also to control mice. All the experimental procedures were performed according to the license for animal experiments (TVA 55.2-1-54-2532-234-2015) granted by the Region of Upper Bavaria.

Organ collection and single cell suspension generation

Blood was aspirated with a syringe from the heart directly after euthanasia. The blood was then placed in a 50 mL tube containing 50 μl of heparin (20 U/mL), mixed and diluted with 20 mL of CB Buffer (PBS + FBS (2%), EDTA (0.4%)). Livers were perfused with 5 mL cold PBS via the portal vein until the liver was opaque. Spleens and thymi were also collected. Every organ was placed in a tube containing CB buffer and kept on ice.

Spleens and thymi were dissociated between two microscopic glass slides. The single cell suspension was resuspended in CB buffer and filtered.

Liver was dissociated with a 70 μm cell strainer. The mononuclear cells were isolated using one of the following methods: 1) the single cell suspension was washed in PBS and resuspended in 6ml of 40% isotonic Easycoll separating solution. 4ml of 80% isotonic Easycoll separating solution was placed in a 15 mL tube, and the single cell suspension solution was carefully overlayered. The samples were centrifuged at RT for 20 min at 900 g (no brakes, no acceleration). The upper layer of hepatocytes was aspirated and the mononuclear cells were isolated from the 40/60% interface; 2) the single cell suspension was washed in MACS buffer (PBS + BSA (0.5%), EDTA (0.4%)) and resuspended in 15 mL of 37% Percoll PLUS. The solution was thoroughly vortexed and centrifuged at RT for 20 min at 900 g (no brakes, no acceleration). The supernatant was carefully aspirated and the cell suspension was washed with CB buffer.

To lyse erythrocytes from spleen, blood and liver, 5 mL of Gey's solution was added to the blood samples. After 5 min, the solution was neutralized with 20 mL of CB Buffer. In the case of blood, the samples were centrifuged and the procedure was repeated. For all the organs, living cells were counted using a Neubauer counting chamber and Trypan Blue.

α-GalCer-loaded CD1d dimer preparation

α-galactosylceramide (α-GalCer) was dissolved in DMSO at a concentration of 1 mg/mL and further diluted to 0.2 mg/mL with PBS containing 0.5% Tween20.

To prepare 50 μl of Dimer-APC staining, 11.2 μl of DimerX I–a recombinant CD1d:Ig fusion protein was mixed with 5.2 μl of diluted α-GalCer and incubated overnight at 37°C. The day after, the α-GalCer-loaded Dimer was labeled with 28 μl of APC Rat Anti-Mouse IgG1 and incubated 1 h at RT. To stop the labeling reaction, 5.6 μl of Purified Mouse IgG1 λ Isotype Control was added to the mix. After 30 min of incubation at RT, the mixture was stored in the fridge. α-Galcer-loaded-dimer-APC was always prepared fresh on the day before the experiment.

Flow cytometry

Four to 8 million cells were stained in 96 well V-bottom plates for flow cytometry analyses. First, cells were washed with PBS and stained with fixable live-dead dye and anti-mouse CD16/CD32 monoclonal antibody, used for blocking the unspecific binding of antibodies to Fc receptors (25 min, 4°C). After washing with FACS buffer (PBS + BSA (0.5%), NaN_3 (0.1%)), the samples were stained with mCD1d-PBS57 tetramer for either 30 min at RT or 20-45 min at 4°C – depending on the batch. In the particular case of *Nr4a3*-Tocky analysis, cells were stained with mCD1d-PBS57 tetramer or α-Galcer-loaded-dimer-APC for 1 h on ice. Cells were then washed and stained with extracellular markers antibodies (20 min, 4°C). In the case of biotinylated antibodies or chemokine receptor antibodies, a 2-step staining was performed. After mCD1d-PBS57 tetramer staining, the samples were incubated with biotinylated antibodies (30 min, 4°C) or chemokine receptor antibodies (40 min, 37°C). In case of S1PR1, cells were stained with anti-$S1P_1$ for

30 min at 4°C, washed and stained with secondary anti-rat FITC antibody (30 min, 4°C). Following the incubation, the cells were washed and stained with the extracellular marker antibody mixture.

Cells were then washed and fixed with either eBioscience™ Foxp3/Transcription Factor Staining Buffer Set (20 min, 4°C) or with a solution of 2% Roti®-Histofix 4% (diluted with PBS) (45 min, 4°C). After the incubation time, cells were washed with Permeabilization Buffer, blocked with anti-CD16/CD32 monoclonal antibody and stained with the intracellular antibody mixture. Samples were intracellularly stained for 1 h at 4°C, washed and stored in the fridge. In case of Roti®-Histofix 4% fixation, the cells were stained overnight.

Samples were acquired with BD FACS Canto™, CytoFLEX S or CytoFLEX LX flow cytometers.

RNA flow cytometry (PrimeFlow)

RNA flow cytometry was performed using the PrimeFlow RNA Assay according to the manufacturer's instructions. Briefly, 5 to 7 million thymocytes were plated in a 96 well V-bottom plate, and cells were stained for live-dead staining, FC block and extracellular markers as described above. Cells were then fixed and permeabilized with the respective buffers according to the protocol, and stained for intracellular markers for 30 min at 4°C. Following additional fixation, hybridization of the target probes *Nr4a1* and *Nfatc1* was performed for 2 h at 40°C in a Thermomix with 96-well plate adaptor and the plate was subsequently stored in the fridge overnight. The following day, signal amplification was performed according to manufacturer's protocol. Samples were acquired with CytoFLEX LX flow cytometer.

Phosflow and endogenous Nur77 staining

Single cell suspension of thymocytes was resuspended in Phosflow buffer (PBS + FBS (0.5%), EDTA (0.4%)) and cells were stained using the BD Pharmingen™ Transcription Factor Phospho (TFP) Buffer Set. Briefly, 5 to 10 million thymocytes were plated in a 96 well V-bottom plate, and cells were stained for live-dead staining, FC block and extracellular markers as described above. Cells were washed with FACS buffer and fixed with 100 μl of 1x TFP Fix/Perm Buffer (50 min, 4°C). After washing with 1x TFP Perm/Wash Buffer, cells were permeabilized with 200 μl of ice-cold Perm III Buffer for 20 min on ice. After the incubation time, cells were washed with 1x TFP Perm/Wash Buffer, blocked with anti-CD16/CD32 monoclonal antibody (15 min, 4°C) and stained with the intracellular antibody mixture containing phospho-specific and/or Nur77 antibodies (O/N, 4°C). The next day, samples were washed and acquired with CytoFLEX LX flow cytometer.

In vivo Bromodeoxyuridine (BrdU) assay

Mice were injected i.p. with 200 μl (2mg) of BrdU solution either 30 min or 4 h before euthanasia. Thymi were collected and processed in order to obtain a single cell suspension. Ten million cells were transferred in a 96-well plate, washed, labeled with live-dead staining, blocked and stained with extracellular antibodies mixture as reported above. Samples were then fixed with 100μl of BD Cytofix/Cytoperm™ Buffer (BD Pharmingen™ BrdU Flow Kit) for 30 min on ice. After washing with diluted BD Perm/Wash™ Buffer (BD Pharmingen™ BrdU Flow Kit), cells were permeabilized with 100 μl of BD Cytoperm™ Permeabilization Buffer Plus (10 min, on ice) (BD Pharmingen™ BrdU Flow Kit), followed by a re-fixation of 5 min (on ice).

In order to render the incorporated BrdU available for labeling, cells were treated with Deoxyribonuclease I (DNase I). DNase I was solubilized with PBS to a final concentration of 1 mg/mL. The working solution consisted of 3 part of DNase solution and 7 part of FACS buffer. After fixation, cells were washed, the supernatant was completely removed and each sample was resuspended in 35 μl of DNase working solution and incubated at 37°C for 1 h. Following incubation, cells were washed wit BD Perm/Wash™ Buffer and stained with 50 μl of intracellular antibody mixture containing anti-BrdU antibody overnight at 4°C. The following day, cells were washed and resuspended in FACS buffer containing the DNA-labeling dye 7-Aminoactinomycin D (7-AAD, dilution 1:200). Samples were acquired in CytoFLEX LX flow cytometer.

Ex vivo cytokine stimulation

Ten to 30 million thymocytes and splenocytes were used for *ex vivo* cytokine stimulation. For each sample, 2/3 of cells were stimulated and 1/3 were used as unstimulated control. Cells were resuspended at a concentration of 10^7 cells/mL in T cell medium (RPMI + FBS (10%), L-Glutamine (1%), HEPES (1%), sodium pyruvate (1%), NEAA (1%), Penicillin-Streptomycin (1%), 2-mercaptoethanol (0.1%)). Phorbol-12-myristat-13-acetat (PMA, 100 ng/mL), ionomycin (1 μM), and monensin (2 μM) were added to the stimulated samples, while the unstimulated controls were only treated with monensin (2 μM). The samples were incubated for 4 h in the incubator at 37°C. Cells were then washed with PBS and stained as described above.

iNKT cell enrichment

For diverse experiments which required sorted cell populations, iNKT cells were enriched by either 1) direct anti-TCR positive enrichment or 2) depletion of CD8+ cells.

1) Single cell suspension of thymocytes were stained with anti-CD16/CD32 monoclonal antibody (15 min, 4°C). After washing, cells were incubated with either mCD1d-PBS57 Tetramer-APC or CD1d-Dimer-APC for 20 min at 4°C or 45min on ice, respectively. Samples were then washed, resuspended in MACS buffer (80 μl/10^6 cells) and labeled with anti-APC MicroBeads

(20 μl/10^6 cells) for 15 min at 4°C. Cell were then washed and resuspended in 500μl of MACS buffer. Enrichment was performed with AutoMACS Pro using the program Possels.

2) Single cell suspension of thymocytes were stained with anti-CD16/CD32 monoclonal antibody (15 min, 4°C). Samples were then washed, resuspended in 500 μl of MACS buffer and labeled with 70 μl of anti-CD8 MicroBeads for 15 min at 4°C. After washing, cells were resuspended in 2 mL of MACS buffer. Enrichment was performed through LS Columns with QuadroMACS.

Cell sorting

Thymic iNKT were pre-enriched with AutoMACS Pro as reported above. The positive (enriched) fraction was stained with extracellular marker antibodies according to the sorting panel. Cells were then resuspended in a solution of FACS Buffer and live-dead dye 7-AAD.

The sorting was performed in a BD FACS Aria™ II, BD FACS Aria™ III or BD FACS Aria™ Fusion. For each sample, 1000 cells were sorted in a well of a 96-well PCR plate pre-filled with 5μl of lysis buffer (2x TCL Buffer (50%), nuclease-free water (49%), 2-mercaptoethanol (Merck, 1%)). When possible, 3 wells were sorted for each population. Plates were sealed, centrifuged and stored at −80°C.

3′ RNA-sequencing

Library preparation for bulk 3′-sequencing of poly(A)-RNA was performed as previously described previously (Parekh et al., 2016). Briefly, frozen cell lysates from sorted cell population (1000 cells) were thawed and RNA was isolated using Agencourt AMPure XP magnetic beads. Barcoded cDNA of each sample was generated with Maxima RT polymerase using oligo-dT primer containing barcodes, unique molecular identifiers (UMIs) and an adaptor. 5′ ends of the cDNAs were extended by a template switch oligo (TSO) and after pooling of all samples, full-length cDNA was purified with Zymoresearch DNA Clean & Concentrator™ according to the manufacturer's protocol. Purified cDNA was amplified with primers binding to the TSO-site and the adaptor. cDNA was tagmented with the Nextera XT kit and 3′ end-fragments finally amplified using primers with Illumina P5 and P7 overhangs. The library was sequenced on a NextSeq 500 (Illumina) with 16 cycles for the barcodes and UMIs and 50 cycles for the cDNA.

3′ RNA-sequencing data analysis

Gencode gene annotations M18 and the mouse reference genome GRCm38 were derived from the Gencode homepage (EMBL-EBI). Dropseq tools v1.12 (Macosko et al., 2015) was used for mapping raw sequencing data to the reference genome. The resulting UMI filtered count matrix was imported into R v3.4.4.

Data analysis was conducted with the following approaches: (I) all samples were used for analysis; (II) control samples ($CD24^+$, NKT1, NKT2 and NKT17) were excluded prior analysis. Hereafter we refer to model 1 for the first approach and model 2 for the latter one.

Prior differential expression analysis with DESeq2 v1.30.1 (Love et al., 2014), dispersion of the data in both models was estimated with a parametric fit using the time point as explanatory variable. Principal component analysis (PCA) was conducted for the rlog transformed data after selecting for the 10 percent most variable genes in model 1. To reduce confounding effects of lowly expressed genes, prior PCA data was filtered for the genes where the sum of counts across all samples was greater than 20 (see Figure 3G).

To define differential expression in both models, no gene filter strategy was applied. To determine genes that were differentially regulated at least at one time point, the LRT test was applied on both models. A gene was considered to be differentially regulated if the adjusted p value was below 0.001 (see Figure 3H, S3E and Table S6). Significant genes from model 2 were clustered using the Euclidian distance metric with the Ward method for agglomeration of genes. The resulting dendrogram was computationally split in 11 subclusters (see Figure S3E) and gene set overrepresentation testing was performed in each subcluster individually with EnrichR (Chen et al., 2013). Spearman correlations of selected transcription factors to all genes within a given cluster were computed and visualized as boxplots (see Figure S3F).

To estimate pairwise fold changes between time points, the Wald test was applied and shrunken apeglm log2 fold changes were calculated afterward (see Table S3).

To determine signature marker genes lists for the NKT1, NKT2 and NKT17 samples, results of the Wald test from model 1 were used. A gene was considered as signature marker gene for a certain population if the apeglm shrunken log2 fold change between the population of interest and all the remaining populations was at least 2 at a fdr alpha level of 0.01 (see Table S7).

Unless differently specified, rlog transformed data was used for heatmap visualization throughout the whole manuscript.

GSVA (Hänzelmann et al., 2013) was conducted on the size factor normalized data as calculated with DESeq2. Pathway definitions for the Reactome database were used as provided by the MsigDB v7.4 (Liberzon et al., 2011; Subramanian et al., 2005) from the Broad Institute (see Figure S2H).

Mathematical estimation of the TCR-stimulus length

To estimate the time period that a single iNKT cell receives TCR signals upon induction, we used the bulk RNA-seq-derived mRNA levels of *Nr4a1*, *Nr4a3* and *Nfatc1* (Figure S2F and Table S4) downstream of TCR stimulus. The data represents the log2 fold-change with respect to double positive (DP) thymocytes. All three kinetics contain information about how long the stimulus signal is present.

However, it is not possible to read off a time-measure that is informative about the per-cell stimulus length. First, because the production of mRNA and degradation on both sides determine the kinetics, and second because cells are formed at different times and we only have a measurement of the bulk.

In order to disentangle these different mechanisms, we fitted a simple transcription model to the data (Figure S2E), given by

$$\dot{N}^{(i)}(t) = r_0^{(i)} + r_{\mathrm{TCR}}(t) - \delta^{(i)} N^{(i)}(t), \tag{1}$$

while the superscript i denotes the molecule species. $N^{(i)}(t)$ represents the number of mRNA copies of molecule i at time t. $r_0^{(i)}$ corresponds to basal transcription that is assumed to be molecule-specific. $r_{\mathrm{TCR}}(t)$ is by definition the TCR-induced part of the transcription, which should be molecule-independent since production of those molecules is subject to the same external stimulus. $\delta^{(i)}$ denotes the degradation rate of molecule species i.

In this analysis we used log2 fold-changes instead of the raw counts for robustness reasons. To calculate those fold-changes in the model, we considered the steady state of Equation (1) by setting $r_{\mathrm{TCR}}(t) = 0$, leading to

$$\dot{N}_{\mathrm{ss}}^{(i)}(t) = r_0^{(i)} - \delta^{(i)} N_{\mathrm{ss}}^{(i)}(t). \tag{2}$$

Equation (2) has an analytical solution that reads

$$N_{\mathrm{ss}}^{(i)}(t) = \frac{r_0^{(i)}}{\delta^{(i)}} + \left(N_0^{(i)} - \frac{r_0^{(i)}}{\delta^{(i)}} e^{-\delta^{(i)} t} \right), \tag{3}$$

where the initial condition is given by $N_0^{(i)} := N^{(i)}(t=0) = 0$. The solution of Equation (1), together with Equation (3) allows for the direct computation of log fold-changes at desired time points.

To infer the stimulus duration, TCR-induced transcription must be parameterized. Here we assume that each cell receives the same stimulus and the spread in signal on the mRNA-level mainly stems from the fact that degradation does not happen instantaneously and that cells are generated non-synchronously. Our TCR-induced transcription $r'_{\mathrm{TCR}j}$ for a single cell j, that was induced at time τ, is assumed to follow a lag-exponential function, given by

$$r'_{\mathrm{TCR}j}(t) = \begin{cases} 0, & t < \tau_j \\ c e^{-k(t-\tau_j)}, & t \geq \tau_j \end{cases}, \tag{4}$$

while c and k parameterize the underlying exponential function. Here we assume explicitly that an iNKT cell receives its stimulus immediately upon generation. This assumption is justified since the concentration of stimulating cells, i.e., DP thymocytes, is much bigger compared to the concentration of iNKT$^{\mathrm{ind}}$ cells. Let $D_{\mathrm{GEN}}(\tau)$ be the distribution of production times τ, then we can write the overall TCR-induced transcription as a weighted composition of elementary functions, i.e.

$$r_{\mathrm{TCR}}(t) = \int_0^\infty \mathrm{d}\tau r'_{\mathrm{TCR}}(t,\tau) D_{\mathrm{GEN}}(\tau). \tag{5}$$

If Equation (5) is plugged into Equation (1), we get a relation between the mRNA molecule kinetics and the decay rate k. TCR-induced transcription and the unknown TCR-stimulus kinetics are strongly linked to each other. Hence the half-life $T_{1/2}^{\mathrm{TCR}} = \frac{\ln(2)}{k}$ defines a timescale on which the TCR-stimulus decays for an individual cell.

To obtain D_{GEN}, we used measurements of iNKT$^{\mathrm{ind}}$ cell numbers at different points in time after tamoxifen administration. First, we calculate the geometric mean of the cell numbers for each point in time (Table S4). Between two points in time we use a linear interpolation. This gives us a function for the accumulated cell count over time. We interpret the last measurement at t = 24 h as a saturation of the cell number, and normalize the curve by its corresponding function value. In this way we obtain an approximation of the cumulative distribution function (CDF) of the mean cell number over time. The (numerical) derivative gives us the desired probability density function of production times, which was called $D_{\mathrm{GEN}}(\tau)$ earlier.

Altogether this leads to a model containing eight parameters: basal transcription and degradation per molecule species and two parameters from the lag-exponential function, the lag being inferred from $D_{\mathrm{GEN}}(\tau)$. In addition, one absolute error σ_{abs} for the log2 fold-changes of the data was introduced as a parameter and assumed to be identical across molecule species. Parameter estimation was performed using least-squares regression. Let θ be the parameter vector and θ_{opt} the set of parameters that globally minimize the negative log-likelihood function. In the presence of one error to be estimated, the overall optimization problem takes the form

$$\theta_{\mathrm{opt}} = \mathrm{argmin}_\theta \left[2n \ln(\sigma_{\mathrm{abs}}(\theta)) + \sum_{i=1}^{n} \left(\frac{y_i - f(x_i,\theta)}{\sigma_{\mathrm{abs}}(\theta)} \right)^2 \right], \tag{6}$$

for n fitted data points y_i with errors σ_{abs}, corresponding model evaluations $f(x_i,\theta)$ and trivial relation $\sigma_{\mathrm{abs}}(\theta) = \theta_j$. The TCR-induced transcription of an exemplary cell (here τ = 13 h) shows a decay rate of k = 0.09 h$^{-1} \Leftrightarrow T_{\frac{1}{2}}^{\mathrm{TCR}}$ = 7.7 h (red dashed line). 95% confidence intervals of the crucial parameter k were calculated using the profile likelihood method, i.e., values for k were fixed around its optimal value and parameter estimation with respect to the remaining parameters was carried out. These bounds translate into bounds for $T_{1/2}^{\mathrm{TCR}}$, given by [6.4 h; 9.3 h] (black dashed lines).

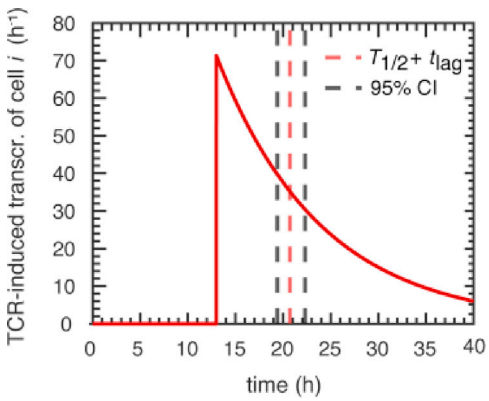

The code was implemented in MATLAB (version R2020a). Parameter estimation was performed with MATLAB's function *lsqnonlin* using the trust-region-reflective algorithm and standard options. Bound constrains for all parameters but the absolute error were set to $[0;\ \infty]$. The error itself was constrained to an interval of $[0;\ 0.3]$, thereby avoiding unrealistically large errors. The system of coupled ordinary differential equations (ODEs) was solved using MATLAB's ODE solver *ode15s*, due to the moderate stiffness of the equations. The implementation of the model is available upon request.

QUANTIFICATION AND STATISTICAL ANALYSIS

Statistical analyses were generated using GraphPad Prism (v7). Details on the statistics used can be found in figure legends and in Table S2. The flow cytometry data were analyzed with FlowJo (v10.5.3). For all of the graphs derived from flow cytometric data, only cell populations with at least 150 recorded events were included. The cell cycle speed analysis was performed as described in (Kretschmer et al., 2020) (Figure 3D, E). The cytokine stimulation assay data were depicted using SPICE software (v6) (Figures 3F and 5A and S7E). Venn diagrams (Figure S5D) were generated using the Venn Diagrams Software (see Key Resources Table). Graphs in Figure 1G (left), 2B, 4B, 6C (bar graphs), S1G, S2A, S2D, S2J, S4H (top), S6C were generated with R (v3.6.3) using homemade scripts and the ggplot2 package (v3.3.3) (Wickham, 2016). Gene expression heatmaps were also generated with R (v3.4.4). All the other graphs were generated with GraphPad Prism (v7).